Lagrangian formulation for finite element analysis of quasi-incompressible fluids with reduced mass losses

Eugenio Oñate[1,2*], Alessandro Franci[1] and Josep M. Carbonell[1,2]

[1] *Centre Internacional de Mètodes Numèrics en Enginyeria (CIMNE)*
Campus Norte UPC, 08034 Barcelona, Spain
www.cimne.com/eo, onate@cimne.upc.edu
[2] *Universitat Politècnica de Catalunya (UPC)*

SUMMARY

We present a Lagrangian formulation for finite element analysis of quasi-incompressible fluids that has excellent mass preservation features. The success of the formulation lays on a new residual-based stabilized expression of the mass balance equation obtained using the Finite Calculus (FIC) method. The governing equations are discretized with the FEM using simplicial elements with equal linear interpolation for the velocities and the pressure. The merits of the formulation in terms of reduced mass loss and overall accuracy are verified in the solution of 2D and 3D quasi-incompressible free-surface flow problems using the Particle Finite Element Method (PFEM, www.cimne.com/pfem). Examples include the sloshing of water in a tank, the collapse of one and two water columns in rectangular and prismatic tanks and the falling of a water sphere into a cylindrical tank containing water. Copyright © 0000 John Wiley & Sons, Ltd.

Received ...

KEY WORDS: Lagrangian formulation, Finite element method, Incompressible flows, Quasi-incompressible flows, Reduced mass loss

1. INTRODUCTION

Preservation of mass is a great challenge in the numerical study of flow problems with high values of the bulk modulus that approach the conditions of incompressibility. Mass losses can be induced by the so-called stabilization terms which are typically added to the discretized form of the momentum and mass balance equations in order to account for high convective effects in the momentum equations in the Eulerian description of the flow, and to satisfy the div-sup condition imposed by the full incompressibility constraint when equal order interpolation of the velocities and the pressure is used in mixed finite element methods (FEM) [1, 5, 43, 44].

An important source of mass loss emanates in the numerical solution of free-surface flows due, among other reasons, to the inaccuracies in predicting the shape of the free-surface during large

*Correspondence to: CIMNE, Edificio C1, Campus Norte, UPC, Gran Capitán s/n, 08034 Barcelona, Spain

flow motions [13]. Mass losses can also occur in the numerical solution of flows with heterogeneous material properties [12] and in homogeneous viscous flows using the Laplace form of the Navier-Stokes equations [17].

Our interest in this work is the modelling and simulation of free surface quasi-incompressible flows accounting for the actual value of the speed of sound in the fluid (or the equivalent bulk modulus) using a particular class of Lagrangian FEM termed the Particle Finite Element Method (PFEM, www.cimne.com/pfem) [2–4], [8]–[14],[16, 18, 19, 27, 28, 30, 32, 34, 35],[39]–[41]. The PFEM treats the mesh nodes in the fluid and solid domains as particles which can freely move and even separate from the main fluid domain representing, for instance, the effect of water drops. A mesh connects the nodes discretizing the domain where the governing equations are solved using a stabilized FEM.

In Lagrangian analysis procedures (such as the PFEM) the motion of fluid particles is tracked during the transient solution. Hence, the convective terms vanish in the momentum equations and no numerical stabilization is needed for treating those terms. Two other sources of mass loss, however, remain in the numerical solution of Lagrangian flows, i.e. that due to the treatment of the incompressibility constraint by a stabilized numerical method, and that induced by the inaccuracies in tracking the flow particles and, in particular, the free surface.

In this work we present a new stabilized Lagrangian formulation for homogeneous quasi-incompressible viscous flows that has excellent mass preservation features. The success of the formulation relies on the consistent derivation of a residual-based stabilized expression of the mass balance equation using the Finite Calculus (FIC) method [7],[20]–[26],[29]–[31],[36, 37].

The FIC approach in mechanics is based on expressing the equations of balance of mass and momentum in a space-time domain of finite size and retaining higher order terms in the Taylor series expansion typically used for expressing the change in the transported variables within the balance domain. In addition to the standard terms of infinitesimal theory, the FIC form of the balance equations contains derivatives of the classical differential equations in mechanics multiplied by characteristic distances in space and time. Examples of stabilized FIC-FEM formulations in fluid and solid mechanics can be found in the references given in the previous paragraph.

In our work we use the second order FIC form in space and the first order FIC form in time of the mass balance equation as the basis for obtaining a new stabilized variational residual expression of that equation useful for finite element analysis. The discretized variational form of the FIC mass balance equation via the FEM introduces terms in the Neumann boundary of the domain and other terms involving the first and second material time derivatives of the pressure that are relevant for ensuring the consistency of the residual formulation. These terms are also crucial for preserving the mass during the transient solution of free surface Lagrangian flows. In addition they allow to compute the nodal pressures from the stabilized mass balance equation without imposing any condition on the pressure at the free surface nodes, thus eliminating another source of mass loss which occurs when the pressure is prescribed to a zero value on the free surface in viscous flows. Numerical tests show that the numerical formulation here presented has an excellent performance in terms of mass conservation and overall accuracy of the solution for free-surface flow problems.

The lay-out of the paper is the following. In the next section we present the basic equations for conservation of linear momentum and mass for a quasi-incompressible fluid in a Lagrangian framework. A full incompressible fluid is considered as a particular limit case of the former.

Next we derive the stabilized FIC form of the mass balance equation. Then the finite element discretization using simplicial element with equal order approximation for the velocity and the pressure is presented and the relevant matrices and vectors of the discretized problem are given. Details of the implicit solution of the Lagrangian FEM equations in time using a Newton iterative scheme are presented. A particular form of the tangent stiffness matrix that accounts for the terms introduced by the bulk modulus of the fluid is presented. The relevance of these terms for enhancing the convergence and overall accuracy of the iterative solution scheme is discussed. The basic steps of the PFEM for solving free-surface flow problems are described.

The efficiency and accuracy of the new stabilized formulation are verified by solving a set of free surface flow problems in two (2D) and three (3D) dimensions with the PFEM. The problems include the sloshing of water in a tank, the motion of a stream within a tank originated by the collapse of a water column, the collision and mixing of two streams due to the collapse of two water columns in a tank and the falling and subsequent penetration of a water sphere into a cylindrical tank containing water. The excellent performance of the numerical method proposed in terms of mass conservation and general accuracy is highlighted.

2. BASIC EQUATIONS

We write the governing equations for a quasi-incompressible Newtonian flow problem in the Lagrangian description as follows [1, 44].

Momentum equations

$$\rho \frac{Dv_i}{Dt} - \frac{\partial \sigma_{ij}}{\partial x_j} - b_i = 0 \quad , \quad i,j = 1, n_s \quad \text{in } \Omega \tag{1}$$

In Eq.(1), Ω is the analysis domain with boundary Γ, v_i and b_i are the velocity and body force components along the ith Cartesian axis, ρ is the density of the fluid, n_s is the number of space dimensions (i.e. $n_s = 3$ for 3D problems) and σ_{ij} are the Cauchy stresses that are split in the deviatoric (s_{ij}) and pressure (p) components as

$$\sigma_{ij} = s_{ij} + p\delta_{ij} \tag{2}$$

where δ_{ij} is the Kronecker delta. Note that the pressure is assumed to be positive for a tension state.

Summation of terms with repeated indices is assumed in Eq.(1) and in the following, unless otherwise specified.

The relationship between the deviatoric stresses and the strain rates has the standard form for a Newtonian fluid,

$$s_{ij} = 2\mu \left(\varepsilon_{ij} - \frac{1}{3}\varepsilon_v \delta_{ij} \right) \tag{3}$$

where μ is the viscosity and the strain rates ε_{ij} are related to the velocities by

$$\varepsilon_{ij} = \frac{1}{2} \left(\frac{\partial v_i}{\partial x_j} + \frac{\partial v_j}{\partial x_i} \right) \tag{4}$$

In Eq.(4) ε_v is the volumetric strain rate defined as

$$\varepsilon_v = \varepsilon_{ii} = \frac{\partial v_i}{\partial x_i} \tag{5}$$

Substituting Eqs.(2) and (4) into (1) gives a useful form of the momentum equations as

$$\rho \frac{Dv_i}{Dt} - \frac{\partial}{\partial x_j}(2\mu\varepsilon_{ij}) + \frac{\partial}{\partial x_i}\left(\frac{2}{3}\mu\varepsilon_v\right) - \frac{\partial p}{\partial x_i} - b_i = 0 \quad , \quad i,j = 1, n_s \tag{6}$$

Remark 1. The term $\frac{Dv_i}{Dt}$ in Eq.(1) is the *material derivative* of the ith velocity component v_i. This term is typically computed in a Lagrangian framework as

$$\frac{Dv_i}{Dt} = \frac{{}^{n+1}v_i - {}^{n}v_i}{\Delta t} \tag{7a}$$

with

$${}^{n+1}v_i := v_i({}^{n+1}\mathbf{x}, {}^{n+1}t) \quad , \quad {}^{n}v_i := v_i({}^{n}\mathbf{x}, {}^{n}t) \tag{7b}$$

where ${}^{n}v_i({}^{n}\mathbf{x}, {}^{n}t)$ is the velocity of the material point that has the position ${}^{n}\mathbf{x}$ at time $t = {}^{n}t$, where $\mathbf{x} = [x_1, x_2, x_3]^T$ is the coordinates vector of a point in a fixed Cartesian system. Note that the convective term, typical of Eulerian formulations, does not appear in the definition of the material derivative [1, 5, 44].

Boundary conditions

The boundary conditions at the Dirichlet (Γ_v) and Neumann (Γ_t) boundaries with $\Gamma = \Gamma_v \cup \Gamma_t$ are

$$v_i - v_i^p = 0 \qquad \text{on } \Gamma_v \tag{8}$$

$$\sigma_{ij} n_j - t_i^p = 0 \qquad \text{on } \Gamma_t \quad i,j = 1, n_s \tag{9}$$

where v_i^p and t_i^p are the prescribed velocities and prescribed tractions on the Γ_v and Γ_t boundaries, respectively [1, 5, 44].

Clearly at a free surface the Neumann boundary conditions typically apply.

For a unloaded free surface $t_i^p = 0$ and the boundary conditions (9) simplify to

$$\sigma_{ij} n_j = 0 \qquad \text{on } \Gamma_t \tag{10}$$

Eq.(10) simplifies further for the inviscid case ($\mu = 0$) using Eqs.(2) and (3) to

$$p = 0 \qquad \text{on } \Gamma_t \tag{11}$$

The use of Eq.(11) on an unloaded free surface instead of Eq.(10) leads to considerable mass losses in numerical solution schemes [13]. In our work the full form of the Neumann boundary condition, as expressed in Eq.(9), is used.

3. MASS BALANCE EQUATION

The standard mass balance equation for a quasi-incompressible fluid can be written as [1, 5, 44]

$$r_v = 0 \tag{12a}$$

with

$$r_v := -\frac{1}{c^2}\frac{Dp}{Dt} + \rho\varepsilon_v \tag{12b}$$

In Eq.(12b) c is the speed of sound in the fluid. For a fully incompressible fluid $c = \infty$ and Eq.(12a) simplifies to the standard form, $\varepsilon_v = 0$. In our work we will retain the quasi-incompressible form of r_v of Eq.(12b) for convenience.

4. STABILIZED FIC FORM OF THE MASS BALANCE EQUATION

Previous stabilized FEM formulations for quasi and fully incompressible fluids and solids were based on the first order form of the Finite Calculus (FIC) balance equation in space [20]–[22],[25],[29]–[31],[36]. In this work we will use the *second order FIC form* of the mass balance equation in space for a quasi-incompressible fluid [36, 37], as well as the first order FIC form of the mass balance equation in time. These forms have the following expressions:

Second order FIC mass balance equation in space

$$r_v + \frac{h_i^2}{12}\frac{\partial^2 r_v}{\partial x_i^2} = 0 \qquad \text{in } \Omega \qquad i = 1, n_s \tag{13}$$

First order FIC mass balance equation in time

$$r_v + \frac{\delta}{2}\frac{Dr_v}{Dt} = 0 \qquad \text{in } \Omega \tag{14}$$

Eq.(13) is obtained by expressing the balance of mass in a rectangular domain of finite size with dimensions $h_1 \times h_2$ (for 2D problems), where h_i are arbitrary distances, and retaining up to third order terms in the Taylor series expansions used for expressing the change of mass within the balance domain. The derivation of Eq.(13) for 2D incompressible flows can be found in [37].

Eq.(14), on the other hand, is obtained by expressing the balance of mass in a space-time domain of infinitesimal length in space and finite dimension δ in time [20]. The derivation of Eqs.(13) and (14) for a 1D problem are shown in the Appendix A.

The FIC terms in Eqs.(13) and (14) play the role of space and time stabilization terms respectively. In the discretized problem, the space dimensions h_i and the time dimension δ are related to characteristic element dimensions and the time step increment, respectively as it will be explained later.

Note that for $h_i \to 0$ and $\delta \to 0$ the standard form of the mass balance equation (12a), as given by the infinitesimal theory, is recovered.

5. FIC FORM OF THE MASS BALANCE EQUATION IN TERMS OF THE MOMENTUM EQUATIONS

From the momentum equations (6) we obtain (neglecting the space changes of the viscosity μ in the term involving ε_v)

$$\frac{2}{3}\mu\frac{\partial\varepsilon_v}{\partial x_i} = -\rho\frac{Dv_i}{Dt} + \frac{\partial}{\partial x_j}(2\mu\varepsilon_{ij}) + \frac{\partial p}{\partial x_i} + b_i = -\rho\frac{Dv_i}{Dt} + \hat{r}_{m_i} \tag{15}$$

From this equation we deduce

$$\frac{\partial\varepsilon_v}{\partial x_i} = \frac{3}{2\mu}\left[-\rho\frac{Dv_i}{Dt} + \hat{r}_{m_i}\right] \tag{16}$$

In the above two equations $\hat{r}_{m_i}$ is a *static momentum term* defined as

$$\hat{r}_{m_i} = \frac{\partial}{\partial x_j}(2\mu\varepsilon_{ij}) + \frac{\partial p}{\partial x_i} + b_i \tag{17}$$

Let us introduce $\frac{\partial\varepsilon_v}{\partial x_i}$ from Eq.(16) into Eq.(13). This gives, using Eq.(12b)

$$\begin{aligned} -\frac{1}{c^2}\frac{Dp}{Dt} + \rho\varepsilon_v - \frac{h_i^2}{12}\frac{\partial^2}{\partial x_i^2}\left(\frac{1}{c^2}\frac{Dp}{Dt}\right) + \frac{h_i^2}{12}\frac{\partial}{\partial x_i}\left(\frac{\partial}{\partial x_i}(\rho\varepsilon_v)\right) = -\frac{1}{c^2}\frac{Dp}{Dt} + \rho\varepsilon_v \\ -\frac{h_i^2}{12}\frac{\partial^2}{\partial x_i^2}\left(\frac{1}{c^2}\frac{Dp}{Dt}\right) + \frac{\rho h_i^2}{8\mu}\frac{\partial}{\partial x_i}\left(-\rho\frac{Dv_i}{Dt} + \hat{r}_{m_i}\right) \end{aligned} \tag{18}$$

In the derivation of Eq.(18), and in the following, we neglect the space changes of c and ρ in the derivatives.

Observation of the term involving the material derivative of v_i in Eq.(18) gives

$$\frac{\partial}{\partial x_i}\left(-\rho\frac{Dv_i}{Dt}\right) = -\rho\frac{D}{Dt}\left(\frac{\partial v_i}{\partial x_i}\right) = -\rho\frac{D\varepsilon_v}{Dt} \tag{19}$$

Substituting Eq.(19) into (18) gives

$$-\frac{1}{c^2}\frac{Dp}{Dt} + \rho\varepsilon_v - \frac{h_i^2}{12c^2}\frac{\partial^2}{\partial x_i^2}\left(\frac{Dp}{Dt}\right) + \frac{\rho h_i^2}{8\mu}\left(-\rho\frac{D\varepsilon_v}{Dt} + \frac{\partial\hat{r}_{m_i}}{\partial x_i}\right) = 0 \tag{20}$$

Expanding the FIC mass balance equation in time (Eq.(14)) gives

$$-\frac{1}{c^2}\frac{Dp}{Dt} + \rho\varepsilon_v - \frac{\delta}{2c^2}\frac{D^2p}{Dt^2} + \frac{\delta}{2}\rho\frac{D\varepsilon_v}{Dt} = 0 \tag{21}$$

From Eq.(21) we deduce

$$-\rho\frac{D\varepsilon_v}{Dt} = -\frac{2}{\delta c^2}\frac{Dp}{Dt} + \frac{2\rho}{\delta}\varepsilon_v - \frac{1}{c^2}\frac{D^2p}{Dt^2} \tag{22}$$

DOI: 10.1002/fld

Substituting Eq.(22) into (20) gives

$$-\frac{1}{c^2}\frac{Dp}{Dt}+\rho\varepsilon_v-\frac{h_i^2}{12c^2}\frac{\partial^2}{\partial x_i^2}\left(\frac{Dp}{Dt}\right)+\frac{\rho h_i^2}{8\mu}\left(-\frac{2}{\delta c^2}\frac{Dp}{Dt}+\frac{2\rho}{\delta}\varepsilon_v-\frac{1}{c^2}\frac{D^2p}{Dt^2}+\frac{\partial\hat{r}_{m_i}}{\partial x_i}\right)=0 \quad (23)$$

In the following we will assume $h_i = h$ where h is a characteristic length that will be related to a typical average dimension of each element in the mesh. Multiplying Eq.(23) by $\frac{8\mu}{\rho h^2}$ gives, after grouping some terms,

$$\boxed{-\frac{1}{\kappa}\frac{Dp}{Dt}+\varepsilon_v-\frac{2\mu\tau}{3\kappa}\frac{\partial}{\partial x_i}\left(\frac{\partial}{\partial x_i}\left(\frac{Dp}{Dt}\right)\right)-\frac{\tau}{c^2}\frac{D^2p}{Dt^2}+\tau\frac{\partial\hat{r}_{m_i}}{\partial x_i}=0} \quad (24)$$

In Eq.(24) $\kappa = \rho c^2$ is the *bulk modulus* of the fluid and τ is a *stabilization parameter* given by

$$\tau=\left(\frac{8\mu}{h^2}+\frac{2\rho}{\delta}\right)^{-1} \quad (25)$$

Remark 2. The coefficient $\frac{2\mu\tau}{3\kappa}$ multiplying the second space derivatives of $\frac{Dp}{Dt}$ in Eq.(24) is much smaller than the coefficients multiplying the rest of the terms in this equation. Numerical tests have shown that the results are not affected by this term. Consequently, this second space derivative term will be neglected in the rest of this work.

Remark 3. The term $\frac{\partial}{\partial x_i}\left(\frac{\partial}{\partial x_j}(2\mu\varepsilon_{ij})\right)$ within $\hat{r}_{m_i}$ in Eq.(24) (see the definition of $\hat{r}_{m_i}$ in Eq.(17)) vanishes for a linear approximation of the velocity field. This is the case for the simplicial elements used in this work.

6. VARIATIONAL EQUATIONS

6.1. Variational expression of the momentum equation

Multiplying Eq.(1) by arbitrary test functions w_i with dimensions of velocity and integrating over the analysis domain Ω gives the weighted residual form of the momentum equations as [1, 5, 44]

$$\int_\Omega w_i\left(\rho\frac{Dv_i}{Dt}-\frac{\partial\sigma_{ij}}{\partial x_j}-b_i\right)d\Omega=0 \quad (26)$$

Integrating by parts the term involving σ_{ij} and using the Neumann boundary conditions (9) yields the weak variational form of the momentum equations as

$$\int_\Omega w_i\rho\frac{Dv_i}{Dt}d\Omega+\int_\Omega\delta\varepsilon_{ij}\sigma_{ij}d\Omega-\int_\Omega w_i b_i d\Omega-\int_{\Gamma_t}w_i t_i^p d\Gamma=0 \quad (27)$$

where $\delta\varepsilon_{ij}=\frac{\partial w_i}{\partial x_j}+\frac{\partial w_j}{\partial x_i}$ is an arbitrary (virtual) strain rate field. Eq.(27) is the standard form of the *principle of virtual power* with the test functions w_i interpreted as "virtual velocities" [1, 5, 44].

DOI: 10.1002/fld

Substituting the expression of the stresses from Eq.(2) into (27) gives

$$\int_\Omega w_i \rho \frac{Dv_i}{Dt} d\Omega + \int_\Omega \left[\delta\varepsilon_{ij} 2\mu \left(\varepsilon_{ij} - \frac{1}{3}\varepsilon_{ii}\delta_{ij} \right) + \delta\varepsilon_v p \right] d\Omega - \int_\Omega w_i b_i d\Omega - \int_{\Gamma_t} w_i t_i^p d\Gamma = 0 \quad (28)$$

Eq.(28) can be written in matrix form as

$$\boxed{\int_\Omega \mathbf{w}^T \rho \frac{D\mathbf{v}}{Dt} d\Omega + \int_\Omega \delta\boldsymbol{\varepsilon}^T \mathbf{D}\boldsymbol{\varepsilon} d\Omega + \int_\Omega \delta\boldsymbol{\varepsilon}^T \mathbf{m} p d\Omega - \int_\Omega \mathbf{w}^T \mathbf{b} d\Omega - \int_{\Gamma_t} \mathbf{w}^T \mathbf{t}^p d\Gamma = 0} \quad (29)$$

In Eq.(29) $\mathbf{w}, \mathbf{v}, \boldsymbol{\varepsilon}$ and $\delta\boldsymbol{\varepsilon}$ are vectors containing the test functions, the velocities, the strain rates and the virtual strain rates respectively; $\mathbf{b}$ and $\mathbf{t}^p$ are body force and surface traction vectors, respectively; $\mathbf{D}$ is the viscous constitutive matrix and $\mathbf{m}$ is an auxiliary vector. These vectors are defined as (for 3D problems)

$$\mathbf{w} = [w_1, w_2, w_3]^T \quad , \quad \mathbf{v} = [v_1, v_2, v_3]^T \quad , \quad \mathbf{b} = [b_1, b_2, b_3]^T \quad , \quad \mathbf{t}^p = [t_1^p, t_2^p, t_3^p]^T$$

$$\boldsymbol{\varepsilon} = [\varepsilon_{11}, \varepsilon_{22}, \varepsilon_{33}, \varepsilon_{12}, \varepsilon_{13}, \varepsilon_{23}]^T \quad , \quad \delta\boldsymbol{\varepsilon} = [\delta\varepsilon_{11}, \delta\varepsilon_{22}, \delta\varepsilon_{33}, \delta\varepsilon_{12}, \delta\varepsilon_{13}, \delta\varepsilon_{23}]^T$$

$$\mathbf{D} = \mu \begin{bmatrix} 4/3 & -2/3 & -2/3 & 0 & 0 & 0 \\ & 4/3 & -2/3 & 0 & 0 & 0 \\ & & 4/3 & 0 & 0 & 0 \\ & & & 2 & 0 & 0 \\ \text{Sym.} & & & & 2 & 0 \\ & & & & & 2 \end{bmatrix} \quad , \quad \mathbf{m} = [1, 1, 1, 0, 0, 0]^T \quad (30)$$

Remark 4. From the definition of $\mathbf{m}$ and $\mathbf{D}$ and Eqs.(2), (3) and (5) we deduce

$$\boldsymbol{\sigma} = \mathbf{s} + \mathbf{m}p \quad , \quad \mathbf{s} = \mathbf{D}\boldsymbol{\varepsilon} \quad \text{and} \quad \varepsilon_v = \mathbf{m}^T \boldsymbol{\varepsilon} \quad (31)$$

where $\boldsymbol{\sigma} = [\sigma_{11}, \sigma_{22}, \sigma_{33}, \sigma_{12}, \sigma_{13}, \sigma_{31}]^T$, and $\mathbf{s} = [s_{11}, s_{22}, s_{33}, s_{12}, s_{13}, s_{23}]^T$ are the stress and deviatoric stress vectors, respectively.

6.2. Variational expression of the stabilized mass balance equation

We multiply Eq.(24) by arbitrary (continuous) test functions q (with dimensions of pressure) defined over the analysis domain Ω. Integrating over Ω gives (neglecting the term involving the second space derivatives of $\frac{Dp}{Dt}$, as mentioned earlier)

$$\int_\Omega -\frac{q}{\kappa}\frac{Dp}{Dt} d\Omega - \int_\Omega q \frac{\tau}{c^2}\frac{D^2 p}{Dt^2} d\Omega + \int_\Omega q\varepsilon_v d\Omega + \int_\Omega q\tau \frac{\partial \hat{r}_{m_i}}{\partial x_i} d\Omega = 0 \quad (32)$$

DOI: 10.1002/fld

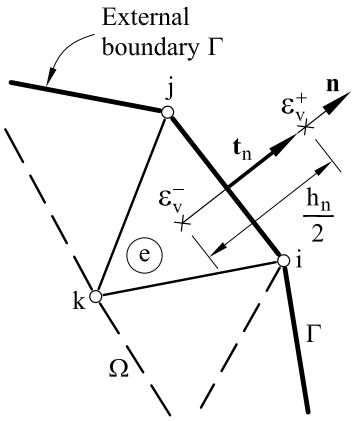

$$\frac{2}{3}\mu\frac{\partial\varepsilon_v}{\partial n}|_{ij} \simeq \frac{2}{h_n}\left(\frac{2}{3}\mu^+\varepsilon_v^+ - \frac{2}{3}\mu^-\varepsilon_v^-\right)$$
$$\varepsilon_v^+ = 0 \quad \text{outside } \Omega$$
$$\frac{2}{3}\mu\frac{\partial\varepsilon_v}{\partial n}|_{ij} \simeq -\frac{4}{3h_n}\mu^-\varepsilon_v^- = -\frac{4}{3h_n}\mu^e\varepsilon_v^e$$

Figure 1. Computation of the term of $\frac{2}{3}\mu\frac{\partial\varepsilon_v}{\partial n}$ at the side ij of a 3-node triangle ijk adjacent to the external boundary Γ

Integrating by parts the last integral in Eq.(32) (and neglecting the space changes of τ) yields

$$\int_\Omega -\frac{q}{\kappa}\frac{Dp}{Dt}d\Omega - \int_\Omega q\frac{\tau}{c^2}\frac{D^2p}{Dt^2}d\Omega + \int_\Omega q\varepsilon_v d\Omega - \int_\Omega \tau\frac{\partial q}{\partial x_i}\hat{r}_{m_i}d\Omega + \underbrace{\int_\Gamma q\tau\hat{r}_{m_i}n_i d\Gamma}_{\mathrm{BT}} = 0 \tag{33}$$

where n_i are the components of the unit normal vector to the external boundary Γ of Ω.

In the derivation of Eq.(33) we have accepted that functions q vanish at any internal element boundary within Ω as it usual in the FEM [1, 5, 44].

Let us consider the boundary term BT in Eq.(33). Using Eq.(16) we deduce

$$BT = \int_\Gamma q\tau\hat{r}_{m_i}n_i d\Gamma = \int_\Gamma q\tau\left(\rho\frac{Dv_i}{Dt} + \frac{2\mu}{3}\frac{\partial\varepsilon_v}{\partial x_i}\right)n_i d\Gamma = \int_\Gamma q\tau\left(\rho\frac{Dv_n}{Dt} + \frac{2\mu}{3}\frac{\partial\varepsilon_v}{\partial n}\right)d\Gamma \tag{34}$$

where $\frac{\partial\varepsilon_v}{\partial n}$ is the derivative of the volumetric strain in the direction of the normal to the external boundary and v_n is the velocity normal to the boundary.

The term $\frac{2\mu}{3}\frac{\partial\varepsilon_v}{\partial n}$ can be approximated as follows

$$\frac{2\mu}{3}\frac{\partial\varepsilon_v}{\partial n} = \frac{2}{h_n}\left(\frac{2}{3}\mu^+\varepsilon_v^+ - \frac{2}{3}\mu^-\varepsilon_v^-\right) \quad \text{at } \Gamma \tag{35}$$

where (μ^+, ε_v^+) and (μ^-, ε_v^-) are respectively the values of μ and ε_v at exterior and interior points of the boundary Γ and h_n is a characteristic length in the normal direction to the boundary. Figure 1 shows an example of the computation of $\frac{2}{3}\mu\frac{\partial\varepsilon_v}{\partial n}$ at the side of a 3-noded triangle adjacent to the external boundary. The same procedure applies for 4-noded tetrahedra.

Clearly, at external boundaries $\varepsilon_v^+ = 0$ and $\varepsilon_v^- = \varepsilon_v$. Hence, ε_v^- coincides with the volumetric strain in the 3-noded triangular element adjacent to the boundary.

Using above argument Eq.(35) simplifies to

$$\frac{2\mu}{3}\frac{\partial\varepsilon_v}{\partial n} = -\frac{4\mu}{3h_n}\varepsilon_v \quad \text{at } \Gamma \tag{36}$$

DOI: 10.1002/fld

On the other hand, the stresses at any boundary satisfy the traction equilibrium condition (9)

$$\sigma_{ij} n_j - t_i = 0 \quad \text{at } \Gamma \tag{37}$$

Substituting Eqs.(2) and (3) into (37) we can rewrite this last equation after multiplying all terms by n_i, as

$$2\mu \frac{\partial v_n}{\partial n} - \frac{2}{3}\mu \varepsilon_v + p - t_n = 0 \quad \text{at } \Gamma \tag{38}$$

where $t_n = t_i n_i$ is the normal traction to the boundary (Figure 1) and $\frac{\partial v_n}{\partial n} = n_i \frac{\partial v_i}{\partial x_j} n_j$.

From Eq.(38) we deduce

$$\frac{2}{3}\mu \varepsilon_v = 2\mu \frac{\partial v_n}{\partial n} + p - t_n \quad \text{at } \Gamma \tag{39}$$

Substituting Eq.(39) into (36) and this one into (34) gives the expression of the boundary integral as

$$BT = \int_\Gamma q\tau \left(\rho \frac{Dv_n}{Dt} - \frac{2}{h_n}(2\mu \frac{\partial v_n}{\partial n} + p - t_n) \right) d\Gamma \tag{40}$$

The normal velocity v_n is fixed at a Dirichlet boundary Γ_v and hence $\frac{Dv_n}{Dt} = 0$ at Γ_v. Also, accepting that $\varepsilon_v = 0$ at Γ_v, the surface tractions at Γ_v coincide precisely with the reactions computed as $t_n = 2\mu \frac{\partial v_n}{\partial n} + p$. Hence, the boundary integral can be neglected at a Dirichlet boundary and, therefore, it has a meaning at a Neumann boundary only. In conclusion,

$$BT = \int_{\Gamma_t} q\tau \left(\rho \frac{Dv_n}{Dt} - \frac{2}{h_n}(2\mu \frac{\partial v_n}{\partial n} + p - t_n) \right) d\Gamma \tag{41}$$

Substituting Eq.(41) into (33) and using the expression of $\hat{r}_{m_i}$ of Eq.(17) yields the variational expression of the stabilized mass balance equation, after rearranging the different terms, as

$$\boxed{\begin{aligned} \int_\Omega \frac{q}{\kappa}\frac{Dp}{Dt} d\Omega + \int_\Omega q \frac{\tau}{c^2}\frac{D^2 p}{Dt^2} d\Omega - \int_\Omega q\varepsilon_v d\Omega + \int_\Omega \tau \frac{\partial q}{\partial x_i}\left(\frac{\partial}{\partial x_i}(2\mu\varepsilon_{ij}) + \frac{\partial p}{\partial x_i} + b_i \right) d\Omega \\ - \int_{\Gamma_t} q\tau \left[\rho \frac{Dv_n}{Dt} - \frac{2}{h_n}(2\mu \frac{\partial v_n}{\partial n} + p - t_n) \right] d\Gamma = 0 \end{aligned}} \tag{42}$$

Expression (42) holds for 2D and 3D problems.

The terms involving the first and second material time derivative of the pressure and the boundary term in Eq.(42) are important to preserve the consistency of the residual form of the FIC mass balance equation. This, in turn, is essential for preserving the conservation of mass in the transient solution of free flow problems. The form of Eq.(42) is a key contribution of the new stabilized formulation, versus previous works on this topic [21, 27, 30, 32, 36, 37, 40].

Remark 5. At an unloaded free surface (Neumann) boundary $t_n = 0$, and hence

$$BT = \int_{\Gamma_t} q\tau \left(\rho \frac{Dv_n}{Dt} - \frac{2}{h_n}(2\mu \frac{\partial v_n}{\partial n} + p) \right) d\Gamma \tag{43}$$

For an inviscid fluid $\mu = 0$ and Eq.(43) simplifies to

$$BT = \int_{\Gamma_t} q\tau \left(\rho \frac{Dv_n}{Dt} - \frac{2p}{h_n} \right) d\Gamma \tag{44}$$

Remark 6. Accounting for the term $\frac{Dv_n}{Dt}$ in the boundary integral of Eq.(42) has proven to be relevant for the enhanced conservation of mass in free surface flows (see Figure 9 in Example 10.1). On the other hand, the effect of the term involving $\frac{D^2p}{Dt^2}$ was negligible in all the problems analyzed in this work.

Remark 7. Eq.(47) is the starting point for deriving a new class of linear triangles with discontinuous pressure field adequate for analysis of incompressible flows with heterogeneous material properties [38].

7. FEM DISCRETIZATION

We discretize the analysis domain into finite elements with n nodes in the standard manner leading to a mesh with a total number of N_e elements and N nodes. In our work we will choose simple 3-noded linear triangles ($n = 3$) for 2D problems and 4-noded tetrahedra ($n = 4$) for 3D problems with local linear shape functions N_i^e defined for each node i ($i = 1, n$) of element e [33, 42]. The velocity components, the test functions and the pressure are interpolated over the mesh in terms of their nodal values in the same manner using the global linear shape functions N_j spanning over the elements sharing node j ($j = 1, N$) [33, 42, 44]. The finite element interpolation can be written in matrix form as

$$\mathbf{v} = \mathbf{N}_v \bar{\mathbf{v}} \ , \ \mathbf{w} = \mathbf{N}_v \bar{\mathbf{w}} \ , \ p = \mathbf{N}_p \bar{\mathbf{p}} \tag{45}$$

where

$$\bar{\mathbf{v}} = \begin{Bmatrix} \bar{\mathbf{v}}^1 \\ \bar{\mathbf{v}}^2 \\ \vdots \\ \bar{\mathbf{v}}^N \end{Bmatrix} \quad \text{with } \bar{\mathbf{v}}^i = \begin{Bmatrix} \bar{v}_1^i \\ \bar{v}_2^i \\ \bar{v}_3^i \end{Bmatrix} \ , \ \bar{\mathbf{w}} = \begin{Bmatrix} \bar{\mathbf{w}}^1 \\ \bar{\mathbf{w}}^2 \\ \vdots \\ \bar{\mathbf{w}}^N \end{Bmatrix} \quad \text{with } \bar{\mathbf{w}}^i = \begin{Bmatrix} \bar{w}_1^i \\ \bar{w}_2^i \\ \bar{w}_3^i \end{Bmatrix} \quad \text{and } \bar{\mathbf{p}} = \begin{Bmatrix} \bar{p}^1 \\ \bar{p}^2 \\ \vdots \\ \bar{p}^N \end{Bmatrix} \tag{46}$$

$$\mathbf{N}_v = [\mathbf{N}_1, \mathbf{N}_2, \cdots, \mathbf{N}_N]^T \ , \ \mathbf{N}_p = [N_1, N_2, \cdots, N_N]^T$$

with $\mathbf{N}_j = N_j \mathbf{I}_n$ where $\mathbf{I}_n$ is the $n \times n$ unit matrix.

In Eq.(46) vectors $\bar{\mathbf{v}}$, $\bar{\mathbf{w}}$ and $\bar{\mathbf{p}}$ contain the nodal velocities, the nodal test functions and the nodal pressures for the whole mesh, respectively and the upperindex denotes the nodal value for each vector or scalar magnitude.

Substituting the FEM approximation (45) into Eqs.(4) and (31) yields the strain rates, the virtual strain rates and the stresses at a point in a mesh in terms of the nodal velocities $\bar{\mathbf{v}}$, the nodal test functions $\bar{\mathbf{w}}$ and the nodal pressures $\bar{\mathbf{p}}$ as

$$\boldsymbol{\varepsilon} = \mathbf{B}\bar{\mathbf{v}} \ , \ \delta\boldsymbol{\varepsilon} = \mathbf{B}\bar{\mathbf{w}} \ , \ \varepsilon_v = \mathbf{m}^T \mathbf{B}\bar{\mathbf{v}} \ , \ \mathbf{s} = \mathbf{D}\mathbf{B}\bar{\mathbf{v}} \ , \ \boldsymbol{\sigma} = \mathbf{D}\mathbf{B}\bar{\mathbf{v}} + \mathbf{m}\mathbf{N}_p\bar{\mathbf{p}} \tag{47}$$

where $\mathbf{B} = [\mathbf{B}_1, \mathbf{B}_2, \cdots, \mathbf{B}_N]$. The expression of $\mathbf{B}_j$ (with index j being a global node number) coincides with the element matrix $\mathbf{B}_i^e$ (with index i being a local node number) of Box 1 changing i by j and N_i^e by N_j.

Substituting the approximations (45) and (47) into Eqs.(29) and (42) and choosing a Galerkin form with $q = N_i$ gives the discretized form of the momentum and (stabilized) mass balance

DOI: 10.1002/fld

equations, after eliminating the arbitrary test functions $\bar{\mathbf{w}}$, as

$$\int_\Omega \mathbf{N}_v^T \rho \mathbf{N}_v \frac{D\bar{\mathbf{v}}}{Dt} d\Omega + \int_\Omega \mathbf{B}^T \mathbf{D}\mathbf{B}\bar{\mathbf{v}} d\Omega + \int_\Omega \mathbf{B}^T \mathbf{m}\mathbf{N}_p \bar{\mathbf{p}} d\Omega - \int_V \mathbf{N}_v^T \mathbf{b} d\Omega - \int_{\Gamma_t} \mathbf{N}_v^T \mathbf{t}^p = 0 \quad (48a)$$

$$\int_\Omega \frac{1}{\kappa} \mathbf{N}_p^T \mathbf{N}_p \frac{D\bar{\mathbf{p}}}{Dt} d\Omega + \int_\Omega \frac{\tau}{c^2} \mathbf{N}_p^T \mathbf{N}_p \frac{D^2\bar{\mathbf{p}}}{Dt^2} d\Omega - \int_\Omega \mathbf{N}_p^T \mathbf{m}^T \mathbf{B}\bar{\mathbf{p}} d\Omega + \int_\Omega \tau (\boldsymbol{\nabla}\mathbf{N}_p)^T (\boldsymbol{\nabla}\mathbf{N}_p \bar{\mathbf{p}} + \mathbf{b}) d\Omega + \\ + \int_{\Gamma_t} \frac{2\tau}{h^n} \mathbf{N}_p^T \mathbf{N}_p \bar{\mathbf{p}} d\Gamma - \mathbf{f}_p = 0 \quad (48b)$$

where

$$\boldsymbol{\nabla}\mathbf{N}_p \equiv [\boldsymbol{\nabla}N_1, \boldsymbol{\nabla}N_2, \cdots, \boldsymbol{\nabla}N_N] \quad \text{with } \boldsymbol{\nabla} = \left\{ \begin{array}{c} \dfrac{\partial}{\partial x_1} \\ \dfrac{\partial}{\partial x_2} \\ \dfrac{\partial}{\partial x_3} \end{array} \right\} \quad (48c)$$

and $\mathbf{f}_p$ includes the boundary terms shown in Box 1. Eqs.(48a,b) can be written in matrix form as

$$\mathbf{M}_0 \dot{\bar{\mathbf{v}}} + \mathbf{K}\bar{\mathbf{v}} + \mathbf{Q}\bar{\mathbf{p}} - \mathbf{f}_v = \mathbf{0} \quad (49a)$$

$$\mathbf{M}_1 \dot{\bar{\mathbf{p}}} + \mathbf{M}_2 \ddot{\bar{\mathbf{p}}} - \mathbf{Q}^T \bar{\mathbf{v}} + (\mathbf{L} + \mathbf{M}_b)\bar{\mathbf{p}} - \mathbf{f}_p = \mathbf{0} \quad (49b)$$

where $\dot{\mathbf{a}}$ and $\ddot{\mathbf{a}}$ denote the first and second material time derivatives of the components of a vector $\mathbf{a}$. The different matrices and vectors in Eqs.(49) are assembled from the element contributions given in Box 1.

Remark 8. The boundary terms of vector $\mathbf{f}_p$ can be incorporated in the different matrices of Eq.(49b). This, however, leads to a non symmetrical set of equations. For this reason we have chosen to compute these boundary terms iteratively within the incremental solution scheme.

Remark 9. The presence of matrix $\mathbf{M}_b$ in Eq.(49b) allows us to compute the pressure without the need of prescribing its value at the free surface. This eliminates the error introduced when the pressure is prescribed to zero in free boundaries, which leads to considerable mass losses in viscous flows. Matrix $\mathbf{M}_b$ was introduced in the discretized stabilized mass balance equation in [13] using a fractional step method and heuristic arguments.

Remark 10. For *transient problems* the stabilization parameter τ of Eq.(25) is computed for each element e using $h = l^e$ and $\delta = \Delta t$ as

$$\tau = \left(\frac{8\mu}{(l^e)^2} + \frac{2\rho}{\Delta t} \right)^{-1} \quad (50)$$

where Δt is the time step used for the transient solution and l^e is a characteristic element length computed as $l^e = 2(\Omega^e)^{1/n_s}$ where Ω^e is the element area (for 3-noded triangles) or volume (for 4-noded tetrahedra). For fluids with heterogeneous material properties the values of μ and ρ in Eq.(50) are computed at the element center.

DOI: 10.1002/fld

$$\mathbf{M}^e_{0_{ij}} = \int_{\Omega^e} \rho N^e_i N_j \mathbf{I}_3 d\Omega \ , \ \mathbf{K}^e_{ij} = \int_{\Omega^e} \mathbf{B}^{eT}_i \mathbf{D} \mathbf{B}^e_j d\Omega \ , \ \mathbf{Q}^e_{ij} = \int_{\Omega^e} \mathbf{B}^{eT}_i \mathbf{m} N^e_j d\Omega$$

$$M^e_{1_{ij}} = \int_{\Omega^e} \frac{1}{\kappa} N^e_i N^e_j d\Omega \ , \ M^e_{2_{ij}} = \int_{\Omega^e} \frac{\tau}{c^2} N^e_i N^e_j d\Omega \ , \ M^e_{b_{ij}} = \int_{\Gamma_t} \frac{2\tau}{h_n} N^e_i N^e_j d\Gamma$$

$$L^e_{ij} = \int_{\Omega^e} \tau (\boldsymbol{\nabla}^T N^e_i) \boldsymbol{\nabla} N^e_j d\Omega \ , \ \mathbf{f}^e_{v_i} = \int_{\Omega^e} \mathbf{N}^e_i \mathbf{b} d\Omega + \int_{\Gamma_t} \mathbf{N}^e_i \mathbf{t} d\Gamma$$

$$f^e_{p_i} = \int_{\Gamma_t} \tau N^e_i \left[\rho \frac{Dv_n}{Dt} - \frac{2}{h_n} (2\mu \varepsilon_n - t_n) \right] d\Gamma - \int_{\Omega^e} \tau \boldsymbol{\nabla}^T N^e_i \mathbf{b} d\Omega$$

with $i, j = 1, n$.
For 3D problems

$$\mathbf{B}^e_i = \begin{bmatrix} \frac{\partial N^e_i}{\partial x_1} & 0 & 0 \\ 0 & \frac{\partial N^e_i}{\partial x_2} & 0 \\ 0 & 0 & \frac{\partial N^e_i}{\partial x_3} \\ \frac{\partial N^e_i}{\partial x_2} & \frac{\partial N^e_i}{\partial x_1} & 0 \\ \frac{\partial N^e_i}{\partial x_3} & 0 & \frac{\partial N^e_i}{\partial x_1} \\ 0 & \frac{\partial N^e_i}{\partial x_3} & \frac{\partial N^e_i}{\partial x_2} \end{bmatrix} \ , \ \mathbf{N}^e_i = N^e_i \mathbf{I}_3 \quad \text{and} \quad \boldsymbol{\nabla} = \begin{Bmatrix} \frac{\partial}{\partial x_1} \\ \frac{\partial}{\partial x_2} \\ \frac{\partial}{\partial x_3} \end{Bmatrix}$$

N^e_i: Local shape function of node i of element e [33, 42]

Box 1. Element form of the matrices and vectors in Eqs.(49)

For *steady state* problems the stabilization parameter is computed as

$$\tau = \left(\frac{8\mu}{(l^e)^2} + \frac{2\rho |\mathbf{v}^e|}{l^e} \right)^{-1} \tag{51}$$

where $\mathbf{v}^e$ is the velocity vector at the element center. Also, the characteristic boundary length h_n in the expression of $\mathbf{f}_p$ (Box 1) has been taken equal to l^e in our computations.

8. INCREMENTAL SOLUTION OF THE DISCRETIZED EQUATIONS

Eqs.(49) are solved in time with an implicit Newton-Raphson type iterative scheme [1, 5, 42, 44]. The basic steps within a time increment $[n, n+1]$ are:

- Initialize variables: $({}^{n+1}\mathbf{x}^1, {}^{n+1}\bar{\mathbf{v}}^1, {}^{n+1}\bar{\mathbf{p}}^1, {}^{n+1}\bar{\mathbf{r}}^1_m) \equiv \{{}^n\mathbf{x}, {}^n\bar{\mathbf{v}}, {}^n\bar{\mathbf{p}}, {}^n\bar{\mathbf{r}}_m\}$.
- Iteration loop: $i = 1, NITER$.
  For each iteration.

DOI: 10.1002/fld

Step 1. Compute the nodal velocity increments $\Delta\bar{\mathbf{v}}$

From Eq.(49a), we deduce

$$^{n+1}\mathbf{H}_v^i \Delta\bar{\mathbf{v}} = -^{n+1}\bar{\mathbf{r}}_m^i \rightarrow \Delta\bar{\mathbf{v}} \tag{52a}$$

with the momentum residual $\bar{\mathbf{r}}_m$ and the iteration matrix $\mathbf{H}_v$ given by

$$\bar{\mathbf{r}}_m = \mathbf{M}_0\dot{\bar{\mathbf{v}}} + \mathbf{K}\bar{\mathbf{v}} + \mathbf{Q}\bar{\mathbf{p}} - \mathbf{f}_v \quad , \quad \mathbf{H}_v = \frac{1}{\Delta t}\mathbf{M}_0 + \mathbf{K} + \mathbf{K}_v \tag{52b}$$

Step 2. Update the nodal velocities

$$^{n+1}\bar{\mathbf{v}}^{i+1} = {}^{n+1}\bar{\mathbf{v}}^i + \Delta\bar{\mathbf{v}} \tag{53}$$

Step 3. Compute the nodal pressures $^{n+1}\bar{\mathbf{p}}^{i+1}$

From Eq.(49b) we obtain

$$^{n+1}\mathbf{H}_p^{i\,n+1}\bar{\mathbf{p}}^{i+1} = \frac{1}{\Delta t}\mathbf{M}_1{}^{n+1}\bar{\mathbf{p}}^i + \frac{1}{\Delta t^2}\mathbf{M}_2(2^n\bar{\mathbf{p}} - {}^{n-1}\bar{\mathbf{p}}) + \mathbf{Q}^{T\,n+1}\bar{\mathbf{v}}^{i+1} + {}^{n+1}\bar{\mathbf{f}}_p^i \rightarrow {}^{n+1}\bar{\mathbf{p}}^{i+1} \tag{54a}$$

with

$$\mathbf{H}_p = \frac{1}{\Delta t}\mathbf{M}_1 + \frac{1}{\Delta t^2}\mathbf{M}_2 + \mathbf{L} + \mathbf{M}_b \tag{54b}$$

Step 4. Update the nodal coordinates

$$^{n+1}\mathbf{x}^{i+1} = {}^{n+1}\mathbf{x}^i + \frac{1}{2}({}^{n+1}\bar{\mathbf{v}}^{i+1} + {}^{n}\bar{\mathbf{v}})\Delta t \tag{55}$$

A more accurate expression for computing $^{n+1}\mathbf{x}^{i+1}$ can be used involving the nodal accelerations [39].

Step 5. Check convergence

Verify the following conditions:

$$\begin{aligned} \|{}^{n+1}\bar{\mathbf{v}}^{i+1} - {}^{n+1}\bar{\mathbf{v}}^i\| &\leq e_v\|{}^{n}\bar{\mathbf{v}}\| \\ \|{}^{n+1}\bar{\mathbf{p}}^{i+1} - {}^{n+1}\bar{\mathbf{p}}^i\| &\leq e_p\|{}^{n}\bar{\mathbf{p}}\| \end{aligned} \tag{56}$$

where e_v and e_p are prescribed error norms for the nodal velocities and the nodal pressures, respectively. In the examples solved in this work we have set $e_v = e_p = 10^{-3}$.

If both conditions (56) are satisfied then make $n \leftarrow n+1$ and proceed to the next time step.

Otherwise, make the iteration counter $i \leftarrow i+1$ and repeat Steps 1–5.

Remark 11. In Eqs.(52)–(56) $^{n+1}(\cdot)$ denotes the values of a matrix or a vector computed using the nodal unknowns at time $n+1$. In our work the derivatives and integrals in the iteration matrices $\mathbf{H}_v$ and $\mathbf{H}_p$ and the residual vector $\bar{\mathbf{r}}_m$ are computed on the *discretized geometry at time* n (i.e. $\Omega^e = {}^n\Omega^e$) while the nodal force vectors $\mathbf{f}_v$ and $\mathbf{f}_p$ are computed on the current

DOI: 10.1002/fld

configuration at time $n+1$. This is equivalent to using an *updated Lagrangian formulation* [1, 43, 44].

Remark 12. The tangent "bulk" stiffness matrix $\mathbf{K}_v$ in the iteration matrix $\mathbf{H}_v$ of Eq.(52b) accounts for the changes of the pressure due to the velocity. Including matrix $\mathbf{K}_v$ in $\mathbf{H}_v$ has proven to be essential for the fast convergence, mass preservation and overall accuracy of the iterative solution. The element expression of $\mathbf{K}_v$ can be obtained as (Appendix B)

$$\mathbf{K}_v^e = \int_{\Omega^e} \mathbf{B}^T \mathbf{m} \theta \Delta t \kappa \mathbf{m}^T \mathbf{B} d\Omega \tag{57}$$

where θ is a positive number such that $0 < \theta \leq 1$ that has the role of preventing the ill-conditioning of the iteration matrix $\mathbf{H}_v$ for very large values of the speed of sound in the fluid that lead to a dominant role of the terms of the tangent bulk stiffness matrix $\mathbf{K}_v$. An adequate selection of θ also improves the overall accuracy of the numerical solution and the preservation of mass for large time steps [8]. For fully incompressible fluids (c and $\kappa = \infty$), a finite value of κ is used in practice in $\mathbf{K}_v$ as this helps to obtaining an accurate solution for velocities and pressure with reduced mass loss in few iterations per time step [8]. These considerations, however, do not affect the value of κ within matrix $\mathbf{M}_1$ in Eq.(49b) that vanishes for the fully incompressible case. Clearly, the value of the terms of $\mathbf{K}_v^e$ can also be limited by reducing the time step size. This, however, leads to an increase in the overall cost of the computations. A similar approach for improving mass conservation in incompressible flows was proposed in [40].

Remark 13. The iteration matrix $\mathbf{H}_v$ in Eq.(52a) is an *approximation of the exact tangent matrix* in the updated Lagrangian formulation for a quasi/fully incompressible fluid [39]. The simplified form of $\mathbf{H}_v$ used in this work has yielded very good results with convergence achieved for the nodal velocities and pressure in 3–4 iterations in all the problems analyzed.

Remark 14. The time step within a time interval $[n, n+1]$ has been chosen as $\Delta t = \min\left(\frac{{}^n l^e_{\min}}{|{}^n\mathbf{v}|_{\max}}, \Delta t_b\right)$ where ${}^n l^e_{\min}$ is the minimum characteristic distance of all elements in the mesh, with l^e computed as explained in Remark 10, $|{}^n\mathbf{v}|_{\max}$ is the maximum value of the modulus of the velocity of all nodes in the mesh and Δt_b is the critical time step of all nodes approaching a solid boundary defined as $\Delta t_b = \min\left(\frac{{}^n l_b}{|{}^n\mathbf{v}_b|_{\max}}\right)$ where ${}^n l_b$ is the distance from the node to the boundary and ${}^n\mathbf{v}_b$ is the velocity of the node. This definition of Δt intends that no node crosses a solid boundary during a time step. Again ${}^n(\cdot)$ denotes values at time $t = {}^n\ t$.

A method that allows using large time steps in the integration of the PFEM equations can be found in [14].

9. ABOUT THE PARTICLE FINITE ELEMENT METHOD (PFEM)

9.1. The basis of the PFEM

Let us consider a domain V containing fluid and solid subdomains. Each subdomain is characterized by a set of points, hereafter termed *particles*. The particles contain all the information for defining

DOI: 10.1002/fld

the geometry and the material and mechanical properties of the underlying subdomain. In the PFEM both subdomains are modelled using an *updated Lagrangian formulation* [1, 43]. That is, all variables are assumed to be known in the *current configuration* at time $n(t = {}^{n}t)$. The new set of variables in the fluid and solid subdomains is sought for the *next or updated configuration* at time $n + 1(t = {}^{n+1}t)$. The FEM is used to solve the equations of continuum mechanics for each of the subdomains. Hence the boundary of each subdomain is identified and then a mesh discretizing these domains is generated in order to solve the governing equations for each subdomain in the standard FEM fashion [1, 5, 33, 42, 44].

The solution steps within a time step in the PFEM are as follows:

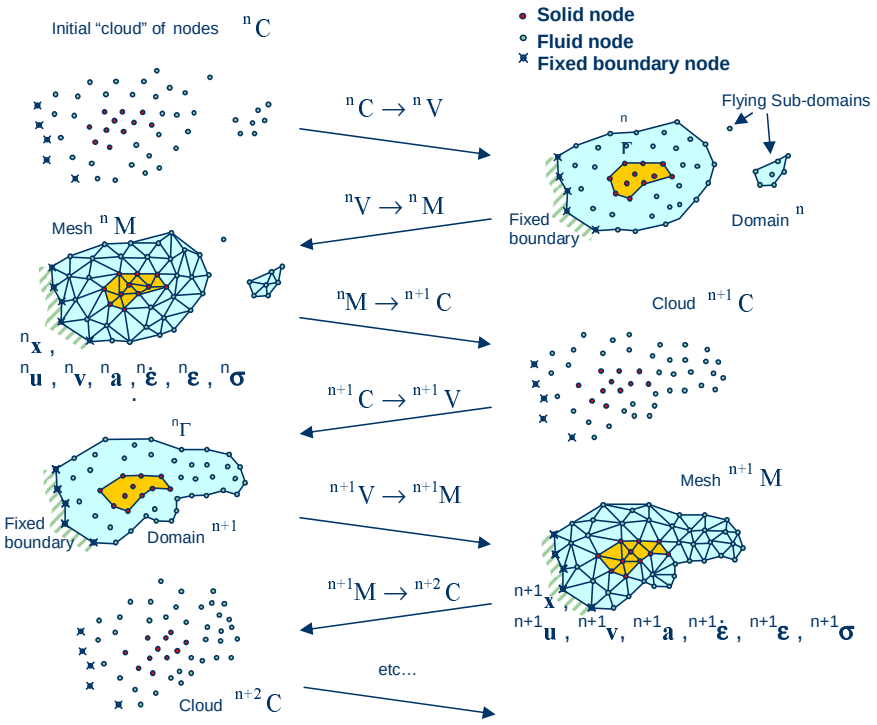

Figure 2. Sequence of steps to update a "cloud" of nodes representing a domain containing a fluid and a solid part from time n ($t = {}^{n}\ t$) to time $n + 2$ ($t = {}^{n}\ t + 2\Delta t$)

1. The starting point at each time step is the cloud of points C in the fluid and solid domains. For instance ${}^{n}C$ denotes the cloud at time $t = {}^{n}t$ (Figure 3).
2. Identify the boundaries defining the analysis domain ${}^{n}V$, as well as the subdomains in the fluid and the solid. This is an essential step as some boundaries (such as the free surface in fluids) may be severely distorted during the solution, including separation and re-entering of nodes. The Alpha Shape method [6] is used for the boundary definition. Clearly, the accuracy in the reconstruction of the boundaries depends on the number of points in the vicinity of each boundary and on the Alpha Shape parameter. In the problems solved in this work the Alpha Shape method has been implementation as described in [10, 27].
3. Discretize the the analysis domain ${}^{n}V$ with a finite element mesh ${}^{n}M$.We use an efficient mesh generation scheme based on an enhanced Delaunay tesselation [9, 10].

DOI: 10.1002/fld

4. Solve the Lagrangian equations of motion for the overall continuum. Compute the state variables in at the next (updated) configuration for ${}^{n}t + \Delta t$: velocities, pressure and viscous stresses in the fluid and displacements, stresses and strains in the solid.
5. Move the mesh nodes to a new position ${}^{n+1}C$ where *n*+1 denotes the time ${}^{n}t + \Delta t$, in terms of the time increment size.
6. Go back to step 1 and repeat the solution for the next time step to obtain ${}^{n+2}C$ (Figure 2).

We note that the key differences between the PFEM and the classical FEM are the remeshing technique and the identification of the domain boundary at each time step.

The quality of the numerical solution depends on the discretization chosen as in the standard FEM. Adaptive mesh refinement techniques can be used to improve the solution.

The CPU time required for meshing grows linearly with the number of nodes. As a general rule, meshing consumes for 3D problems around 15% of the total CPU time per time step, while the solution of the equations (with typically 3 iterations per time step) and the system assembly consume approximately 70% and 15% of the CPU time per time step, respectively. These figures refer to analyses in a single processor Pentium IV PC [35]. Considerable speed can be gained using parallel computing techniques.

In this work we will apply the PFEM to problems involving a rigid domain containing fluid particles only. Application of the PFEM in fluid and solid mechanics and in fluid-structure interaction problems can be found in [2–4], [8]–[14],[16, 18, 19, 27, 28, 30, 32, 34, 35],[39]–[41], as well in www.cimne.com/pfem.

9.2. Treatment of contact conditions in the PFEM

Known velocities at boundaries in the PFEM are prescribed in strong form to the boundary nodes. These nodes might belong to fixed external boundaries or to moving boundaries linked to the interacting solids. Surface tractions are applied to the Neumann part of the boundary, as usual in the FEM.

Contact between fluid particles and fixed boundaries is accounted for by the incompressibility condition which naturally prevents fluid nodes to penetrate into the solid boundaries [10, 27, 32, 35].

The contact between two solid interfaces is treated by introducing a layer of *contact elements* between the two interacting solid interfaces. This contact layer is *automatically created during the mesh generation step* by prescribing a minimum distance (h_c) between two solid boundaries. If the distance exceeds the minimum value (h_c) then the generated elements are treated as fluid elements. Otherwise the elements are treated as contact elements where a relationship between the tangential and normal forces and the corresponding displacement is introduced [27, 32, 35] (Figure 3).

This algorithm allows us to model complex frictional contact conditions between two or more interacting bodies moving in water in an a simple manner. The algorithm has been used to model frictional contact situations between rigid or elastic solids in structural mechanics applications, such as soil/rock excavation problems [2, 3]. The frictional contact algorithm described above has been extended by Oliver *et al.* [18, 19] for analysis of metal cutting and machining problems.

DOI: 10.1002/fld

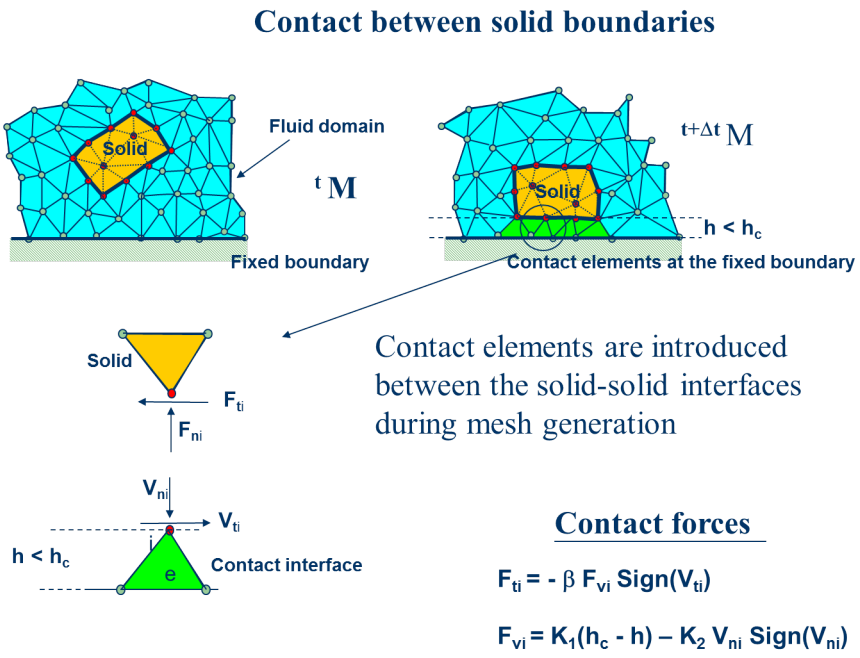

Figure 3. Modelling of contact conditions at a soil-solid interface with the PFEM

10. EXAMPLES

10.1. Sloshing of water in prismatic tank

The problem has been solved first in 2D. Figure 4 shows the geometry of the tank, the material properties, the time step size and the initial mesh of 5064 3-noded triangles discretizing the interior fluid. The fluid oscillates due to the hydrostatic forces induced by its original position.

The problem has been run using different values of the parameter θ influencing the condition number of the tangent bulk stiffness matrix $\mathbf{K}_v^e$ (see Eq.(57) and Appendix B). The first set of results (Figures 5–9) were obtained with $\theta = 1$. The problem was then solved for $\theta = 0.08$, thereby, reducing in one order the magnitude of the diagonal terms in $\mathbf{K}_v^e$.

Figure 5 shows snapshots of the water geometry at different times. Pressure contours are superposed to the deformed geometry of the fluid in the figures.

The convergence of the iterative scheme for a typical time step is shown in Figure 6. Convergence for the velocity and the pressure is found in less than 4 iterations for all time steps.

Figure 7 shows the evolution of the percentage of water volume (i.e. mass) loss introduced by the numerical solution scheme. The accumulated volume loss (in percentage versus the initial volume) for the method proposed with $\theta = 1$ is approximately 1.33% over 20 seconds of simulation time (Figure 7a). The average volume variation in absolute value per time step is $1.09 \times 10^{-4}\%$ (Figure 7b). The total water volume loss is the sum of the losses induced by the numerical scheme and the losses due to the updating of the free surface using the PFEM (Section 9.1). No correction of mass has been introduced at the end of each time step. Taking all this into account, the fluid volume loss over the analysis period is remarkably low.

DOI: 10.1002/fld

As mentioned earlier, the volume losses induced by the free surface updating can be reduced using a finer mesh in that region in conjunction with an enhanced alpha shape technique.

Figure 8 shows that the total fluid volume loss can be reduced to almost zero by introducing a small correction in the free surface at the end of each time step.

The fluid volume losses obtained using a standard first order fractional step method and the PFEM (Appendix C) are shown in Figure 7a for comparison. Clearly the method proposed in this paper leads to a reduction in the overall fluid volume loss, as well as in the volume loss per time step.

The positive effect of accounting for the normal acceleration term $\frac{Dv_n}{Dt}$ in the boundary integral of Eq.(41) in terms of volume preservation is shown in Figure 9. Curve (a) in the figure shows that the accumulated volume variation over 20 seconds using the full formulation amount to 2.18%. If the $\frac{Dv_n}{Dt}$ term is neglected the percentage of volume loss reaches 3.3% in the same period (curve (b)). These figures do not include any volume correction in the free surface at each time step.

Figure 10 shows a comparison between the fluid volume loss for $\theta = 1$ and $\theta = 0.08$ using the same time step in both cases ($\Delta t = 10^{-3}s$). Results show that the reduction of the tangent bulk stiffness matrix terms leads to an improvement in the preservation of the initial volume of the fluid. It is noted that the convergence of the iterative solution for $\theta = 0.08$ was the same as for $\theta = 1$.

Figure 11 shows that a similar improvement in the volume preservation can be obtained using $\theta = 1$ and reducing the time step to $\Delta t = 10^{-4}s$. This, however, increases the cost of the computations.

These results indicate that accurate numerical results with reduced volume losses can be obtained by appropriately adjusting the parameter θ in the tangent bulk modulus matrix while keeping the time step size to competitive values in terms of CPU cost. A study of the influence of θ in the numerical solution for quasi-incompressible free surface fluids in terms of volume preservation and overall accuracy using the formulation here presented can be found in [8].

Figures 12 and 13 show a similar set of results for the 3D analysis of the same sloshing problem using a relative coarse initial mesh of 106771 4-noded tetrahedra and $\theta = 1$. It is remarkable that the percentage of total fluid volume loss due to the numerical scheme after 10 seconds of analysis is approximately 1%.

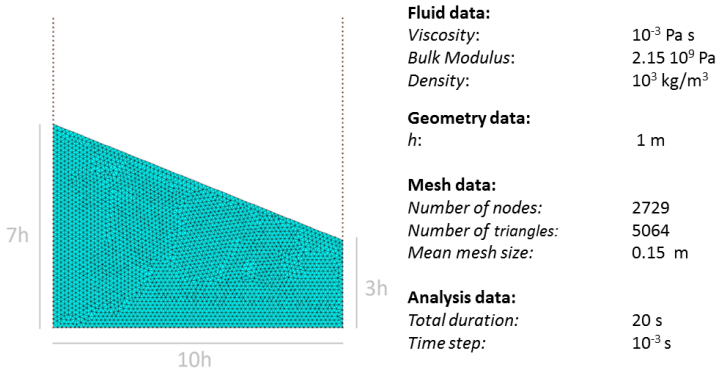

Figure 4. 2D analysis of sloshing of water in rectangular tank. Initial geometry, analysis data and mesh of 5064 3-noded triangles discretizing the water in the tank

DOI: 10.1002/fld

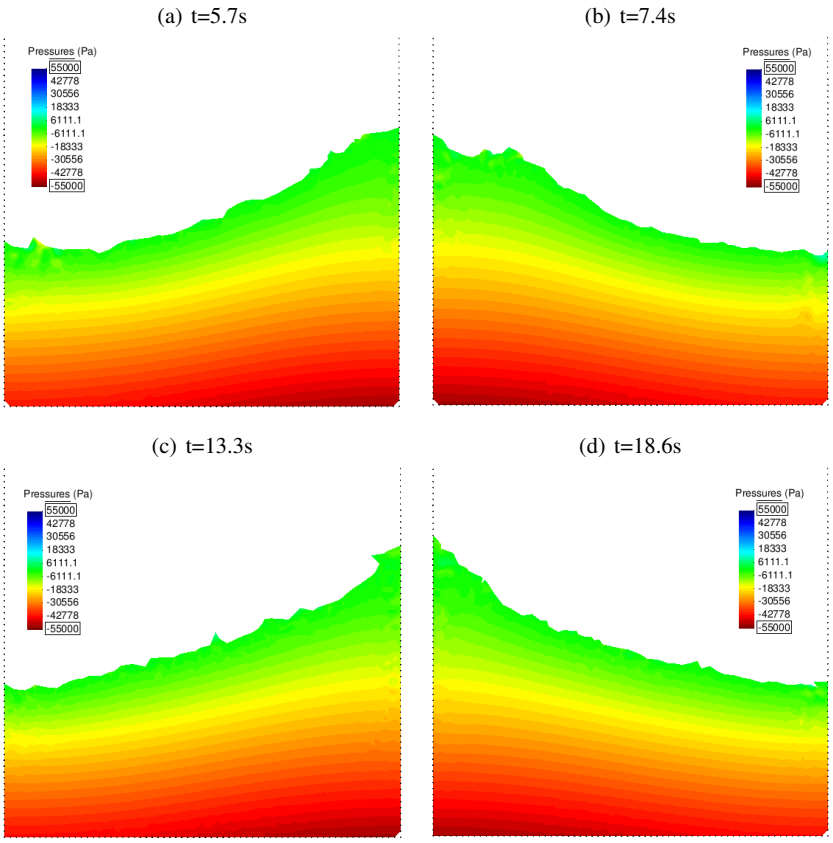

Figure 5. 2D sloshing of water in rectangular tank. Snapshots of water geometry at two different times ($\theta = 1$). Colours indicate pressure contours

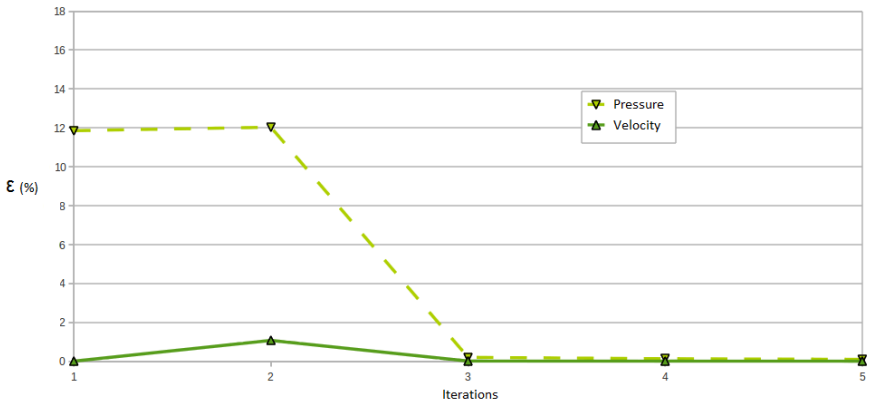

Figure 6. 2D sloshing of water in rectangular tank. Convergence of velocity and pressure at a certain time of the analysis ($\theta = 1$)

10.2. Collapse of water column in prismatic tank with internal rigid step

The geometry of the water column, the tank and the internal step are shown in Figure 14 together with the initial mesh of 3880 3-noded triangles, the material properties and the analysis data. The problem was solved with the new method proposed with $\theta = 1$. The effect of the surrounding air has not been taken into account in the 2D analysis.

DOI: 10.1002/fld

Collapse of the water column is induced by instantaneously removing the vertical wall retaining the water. This originates the flow of water within the tank, the formation of a jet after the water stream hits the rigid step and the subsequent sloshing of the fluid as it impacts the tank walls.

Figure 15 shows the evolution of the water stream at different times. The contour of the velocity modulus are superposed over the fluid domain.

Figure 16a shows that the percentage of initial water volume loss over 2 seconds of simulation time is negligible. The percentage of volume loss per time step is 9.86 $\times 10^{-4}$ (Figure 16b). This is remarkably low for a problem of this complexity. We note that no mass correction has been introduced at the end of each time step.

Figures 17–20 show a similar set of results for the same problem solved in 3D using the same method and an initial mesh of 132956 4-noded tetrahedra discretizing both the water and the air domain. The qualitative agreement of numerical results with the experimental ones shown in Figure 19 [15] is noticeable despite the coarseness of the mesh used. The accumulated fluid volume loss (in percentage) introduced by the numerical algorithm after 0.4 seconds of analysis is $\simeq 2\%$. The average percentage of volume loss per time step is $1.71 \times 10^{-4}\%$ (Figure 20).

Convergence of the numerical solution was again found in less than four iterations per time step for the 2D and 3D solutions.

10.3. Impact and mixing of fluids after collapse of two water columns in a rectangular tank

This problem simulates the 2D motion, impact and subsequent mixing of two fluid streams originated by the collapse of two water columns located at the end sides of a rectangular tank.

Figure 21 shows the initial geometry of the tank, the two water columns, the initial mesh of 3988 3-noded triangles chosen for discretizing the two columns, the fluid properties and the analysis data. The effect of the surrounding air was not taken into account in the analysis. The problem was solved using the method proposed in the paper with $\theta = 1$.

Figure 22 shows snapshots of the motion of the water columns after removal of the retaining walls. Alter a few instants the two water streams impact with each other and mix as shown in the figure.

The evolution of the percentage of the initial fluid volume loss over the simulation time is shown in Figure 23. A maximum of 2.8% of the initial fluid volume is lost over eight seconds of analysis. This can be considered a low value for a problem of this complexity. No mass correction was introduced during the simulation to compensate any volume losses.

10.4. Falling of a water sphere in a cylindrical tank containing water

The final example is the 3D analysis of the impact of a sphere made of water as it falls in a cylindrical tank containing water. Both the water in the sphere and in the tank mix in a single fluid after the impact. Figure 24 shows the material and analysis data and the initial discretization of the sphere, the water in the tank and the air in 88892 4-noded tetrahedra. The problem was solved with the new stabilized method presented in the paper with $\theta = 1$. Figure 25 shows snapshots of the mixing process at different times. An average of four iterations for convergence of the velocity and the pressure were needed during all the steps of the analysis. The total water mass lost in the sphere and the tank due to the numerical algorithm was $\simeq 2\%$ after 3 seconds of analysis (Figure 26a).

DOI: 10.1002/fld

(a) Accumulated volume loss over 20 seconds of analysis

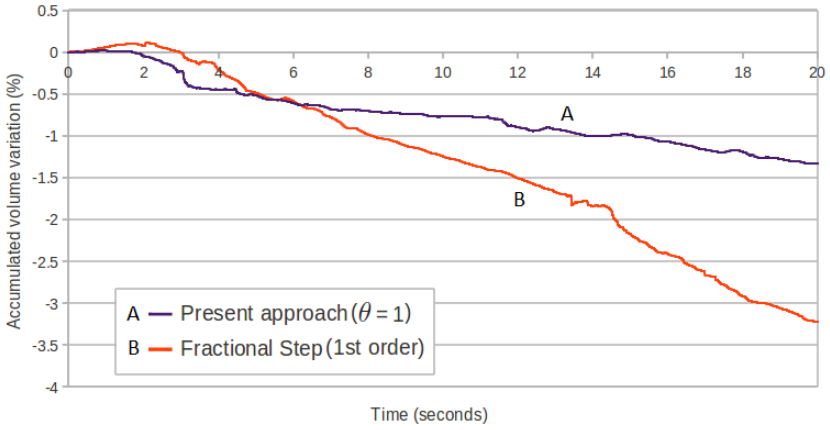

(b) Volume variation (in %) per time step over 20 seconds of analysis (Current method)

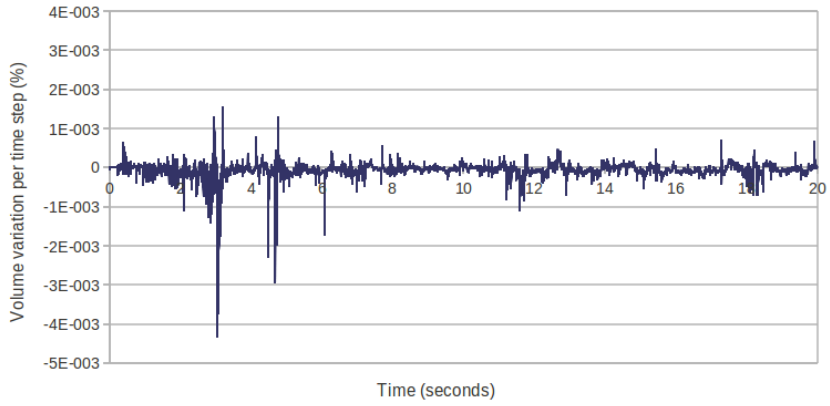

Figure 7. 2D sloshing of water in rectangular tank. (a) Time evolution of the percentage of water volume loss due to the numerical algorithm. (b) Volume variation per time step. Average value. Current method. 1.09×10^{-4}%. Fractional step: 2.07×10^{-4}%.

DOI: 10.1002/fld

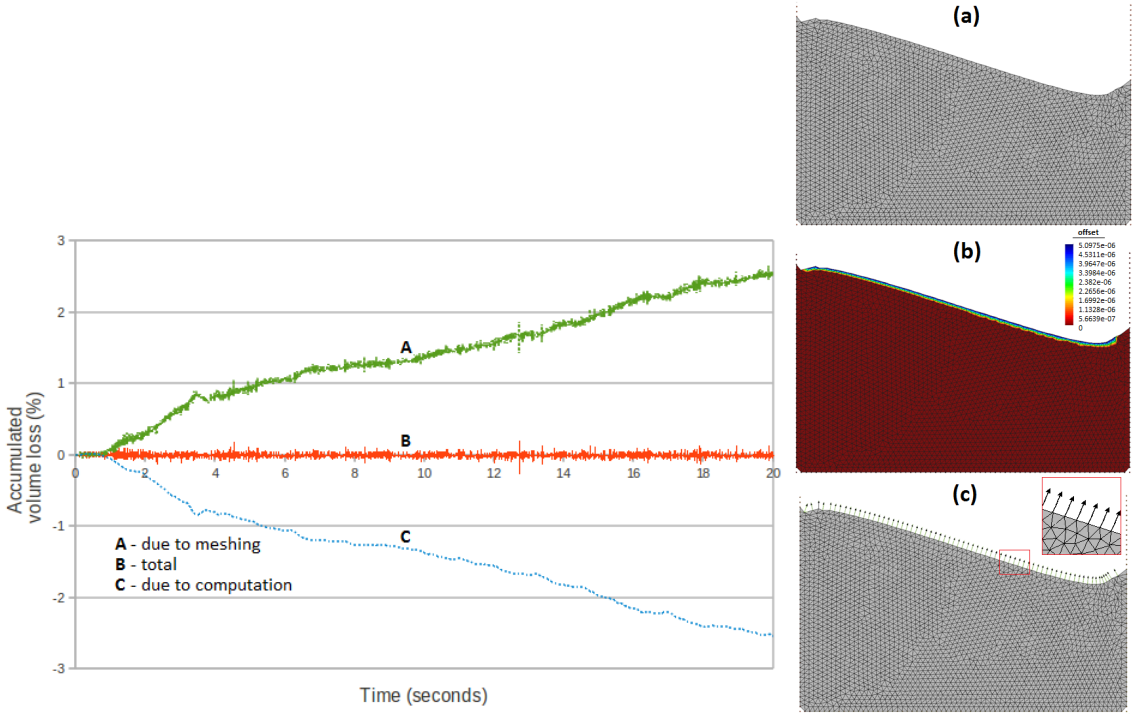

Figure 8. 2D sloshing of water in rectangular tank ($\theta = 1$). Recovery of initial fluid volume by correcting the free surface at mesh generation level. Right figures: (a) Compute total volume variation (ΔV) before remeshing. (b) Compute free surface offset = $\frac{\Delta V}{L_{\text{free surface}}}$. (c) Move free surface nodes in the normal direction to the boundary a distance equal to the offset computed in b)

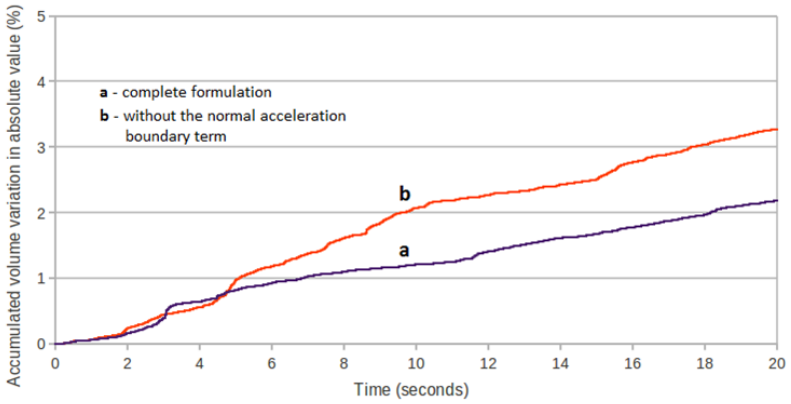

Figure 9. 2D sloshing of water in rectangular tank ($\theta = 1$). Accumulated fluid volume loss (in %) over time using the full stabilized formulation (curve a) and neglecting the normal acceleration term $\frac{Dv_n}{Dt}$ in the expression of $\mathbf{f}_p$ (curve b)

DOI: 10.1002/fld

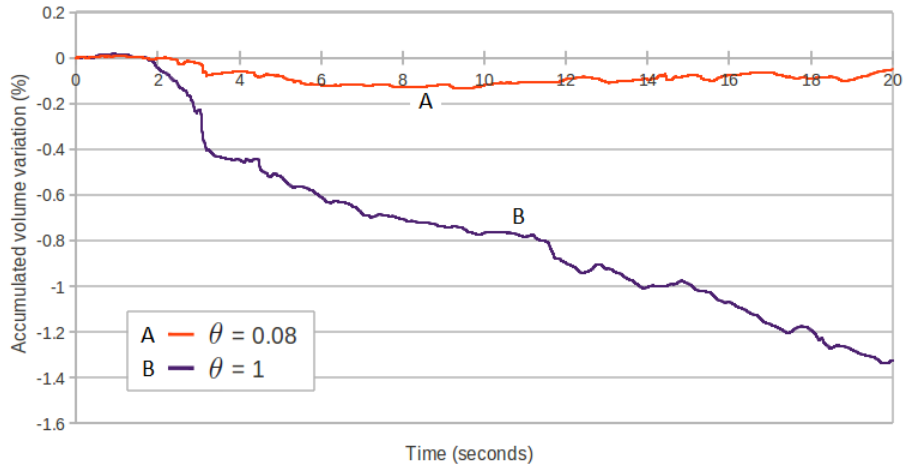

Figure 10. 2D sloshing of water in rectangular tank. Time evolution of percentage of water volume loss obtained using the current method with $\theta = 0.08$ (curve A) and $\theta = 1$ (curve B) $\Delta t = 10^{-3}s$

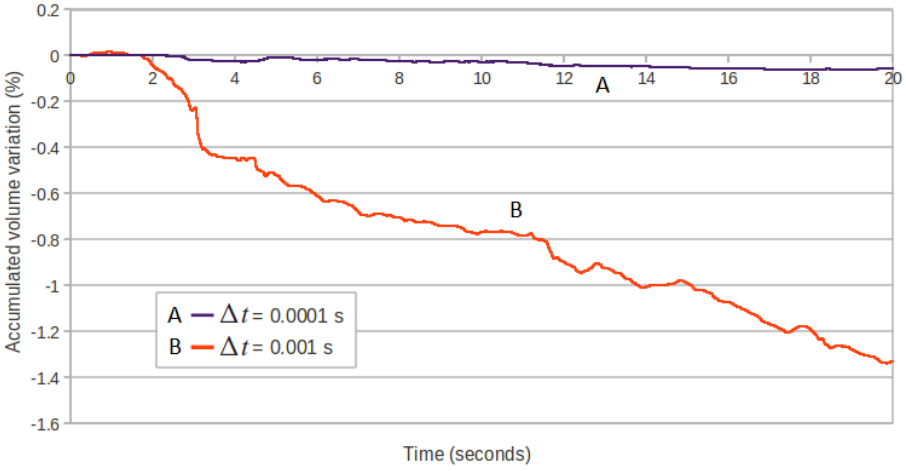

Figure 11. 2D sloshing of water in rectangular tank. Time evolution of percentage of value loss obtained with the current method. Curve A: $\theta = 1$ and $\Delta t = 10^{-4}s$. Curve B: $\theta = 1$ and $\Delta t = 10^{-3}s$

DOI: 10.1002/fld

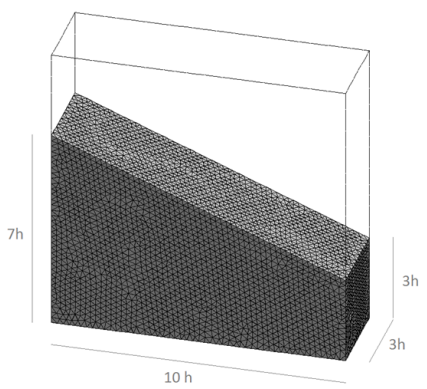

Fluid data:

Viscosity:	10^{-3} Pa s
Bulk Modulus:	2.15 10^{9} Pa
Density:	10^{3} kg/m^{3}

Geometry data:

h:	1 m

Mesh data:

Number of nodes:	23763
Number of tetrahedra:	106771
Mean mesh size:	0.2 m

Analysis data:

Total duration:	10s
Time step:	10^{-3} s

(a) t=5.7s (b) t=7.4s

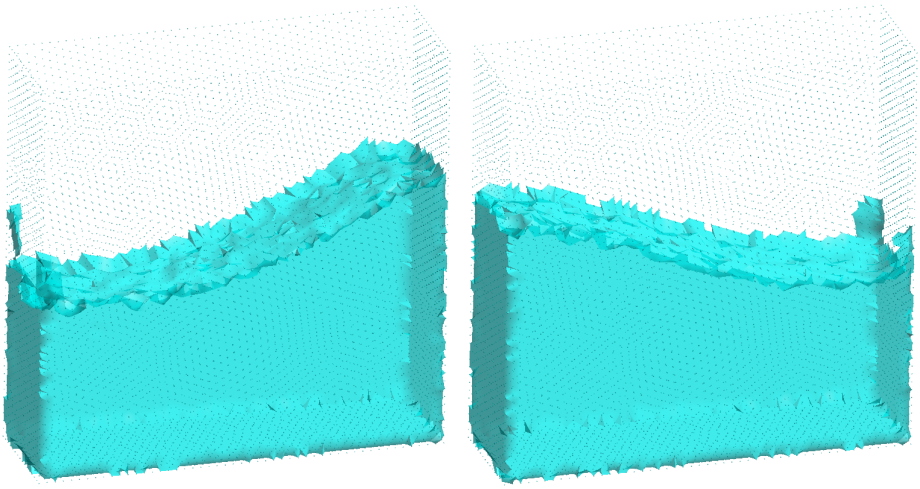

Figure 12. 3D analysis of sloshing of water in prismatic tank ($\theta = 1$). Initial geometry, analysis data and snapshots of water geometry at two different times ($t = 5.7$s left and $t = 7.4$s right)

DOI: 10.1002/fld

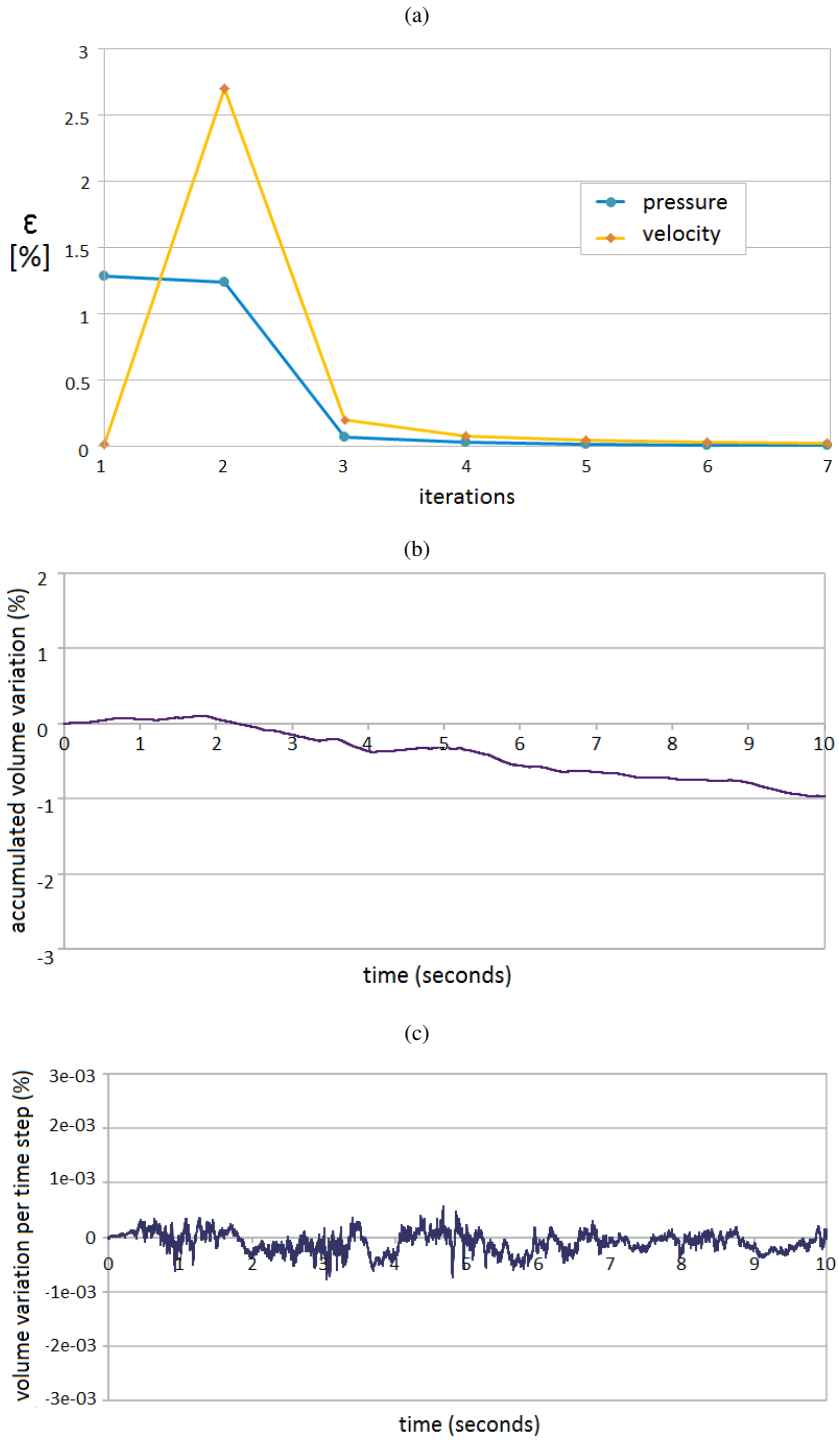

Figure 13. 3D analysis of sloshing of water in prismatic tank ($\theta = 1$). (a) Convergence of velocities and pressure for a certain time step. (b) Time evolution of accumulated water volume loss (in percentage) due to the numerical algorithm. (c) Volume loss (in %) per time step over 2 seconds of analysis. Average volume loss per time step: $1.64 \times 10^{-4}\%$

DOI: 10.1002/fld

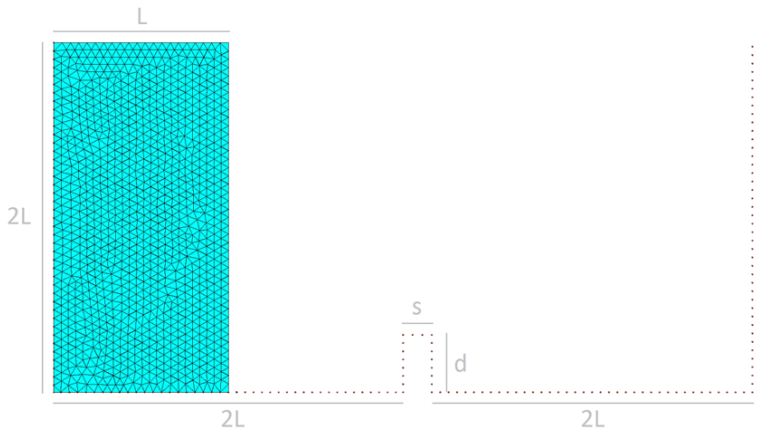

Fluid data:	**Geometry data:**	**Mesh data:**	**Analysis data:**
Viscosity: 10^{-3} Pa s	*L*: 0.146 m	*Number of nodes:* 2194	*Total duration:* 2 s
Bulk Modulus: 2.15 10^{9} Pa	*s*: 0.024 m	*Number of triangles:* 3880	*Time step:* 10^{-4} s
Density: 10^{3} kg/m^{3}	*d*: 0.048 m	*Mean mesh size:* 0.005 m	

Figure 14. 2D collapse of water column in rectangular tank containing a rigid step. Geometry, analysis data and initial mesh of 3880 3-noded triangles discretizing the water column ($\theta = 1$)

DOI: 10.1002/fld

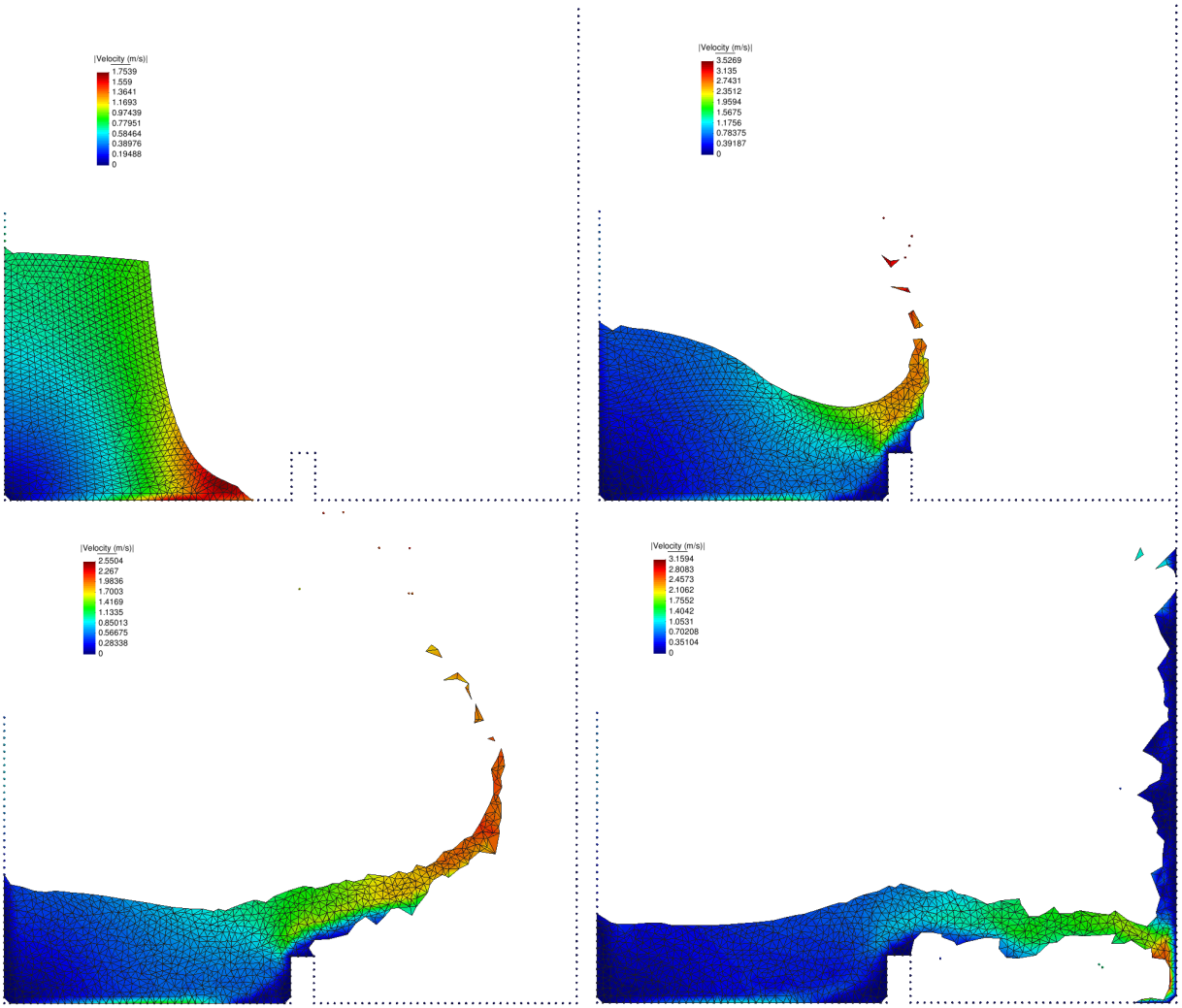

Figure 15. 2D collapse of water column. Snapshots of water flow at different times ($t = 0.1$s, $t = 0.2$s, $t = 0.3$s, $t = 0.4$s). Results for $\theta = 1$

DOI: 10.1002/fld

(a)

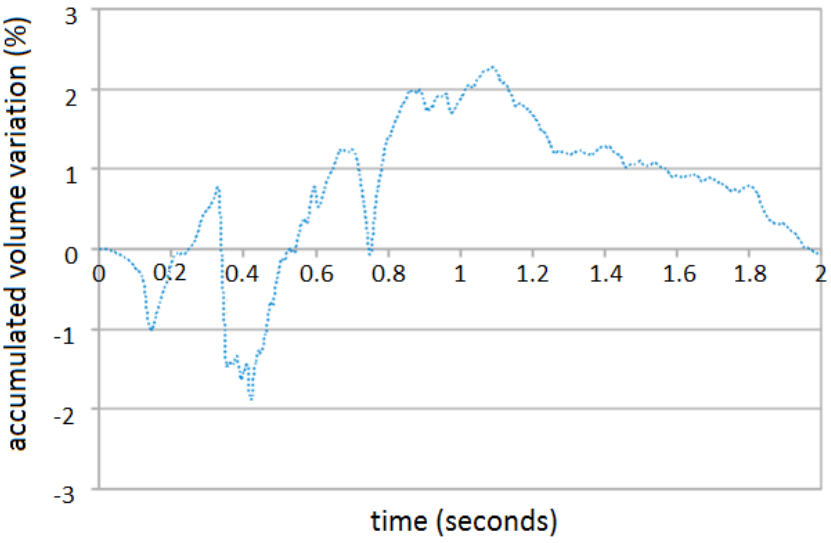

(b)

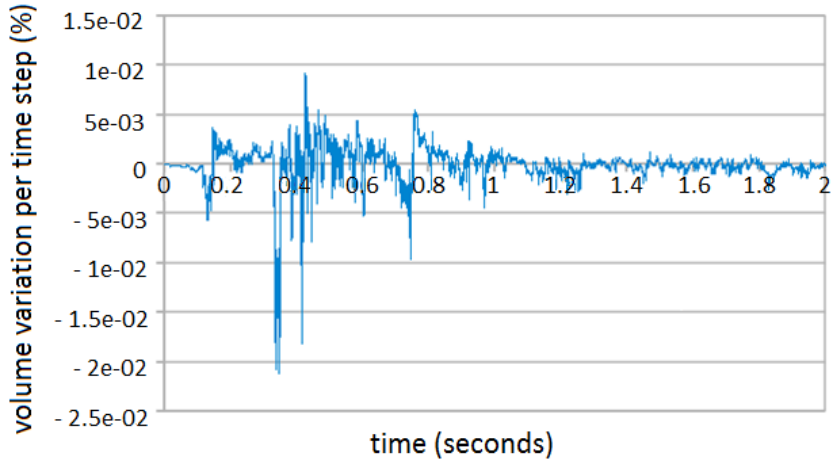

Figure 16. 2D collapse of water column. (a) Accumulated volume loss (in percentage) over two seconds of analysis due to the numerical algorithm. (b) Volume loss (in %) per time step. Average volume variation in a time step: $9.86\times10^{-4}\%$. Results for $\theta = 1$

DOI: 10.1002/fld

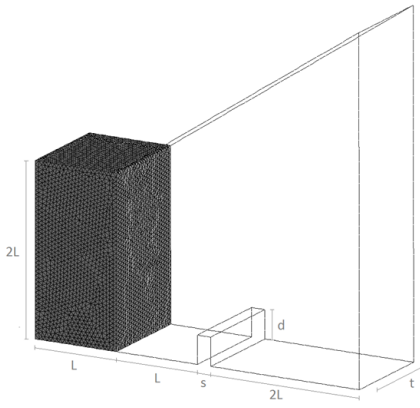

Fluid data:

Viscosity:	10^{-3} Pa s
Bulk Modulus:	2.15 10^{9} Pa
Density:	10^{3} kg/m^{3}

Geometry data:

L:	0.146 m
s:	0.024 m
d:	0.048 m
t:	0.175 m

Mesh data:

Number of nodes:	54918
Number of tetrahedra:	132956
Mean mesh size:	0.007 m

Analysis data:

Total duration:	0.5 s
Time step:	10^{-4} s

Figure 17. 3D collapse of water column in prismatic tank containing a rigid step. Analysis data and initial geometry of the analysis domain chosen for discretizing the column and the surrounding air

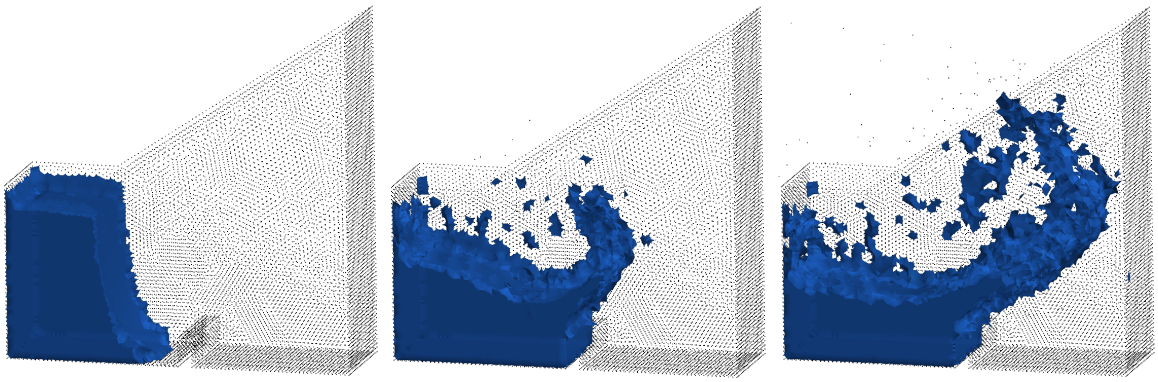

Figure 18. 3D collapse of water column. Evolution of the water flow at different times $t = 0.1$s, $t = 0.2$s, $t = 0.3$s. The effect of the surrounding air has been taken into account in the analysis. Results for $\theta = 1$

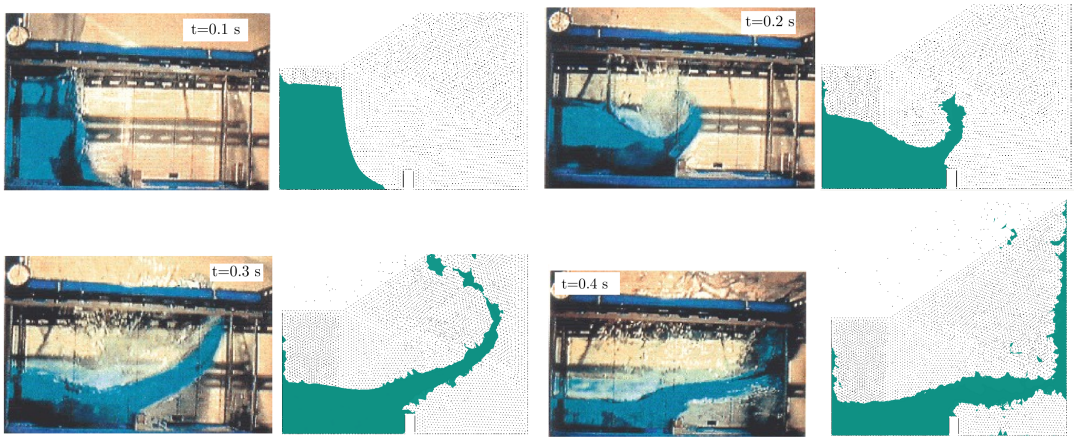

Figure 19. Collapse of water column. Comparison between experimental and 3D PFEM results at different times ($\theta = 1$)

DOI: 10.1002/fld

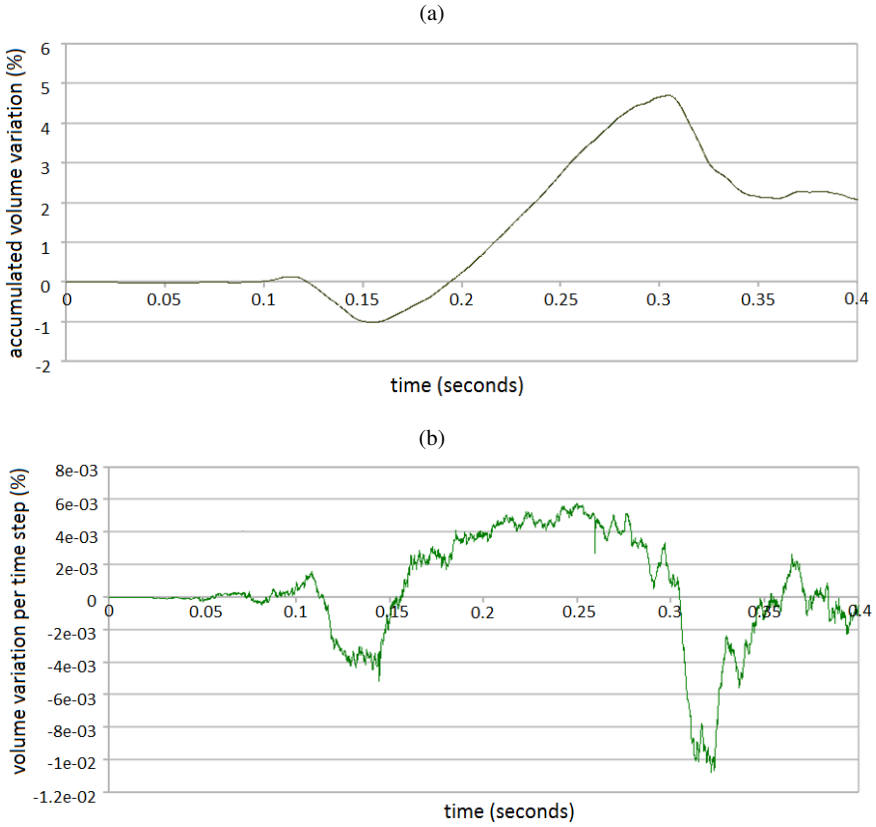

Figure 20. 3D collapse of water column. (a) Accumulated volume loss (in percentage) over 0.4 seconds of analysis due to the numerical algorithm. (b) Volume loss (in %) per time step. Average volume variation in a time step: $1.71 \times 10^{-4}\%$. Results for $\theta = 1$

Fluid data:
Viscosity: 10^{-3} Pa s
Bulk Modulus: 2.15 10^{9} Pa
Density: 10^{3} kg/m^{3}

Geometry data:
L: 0.5 m

Mesh data:
Number of nodes: 2261
Number of triangles: 3988
Mean mesh size: 0. 75 m

Analysis data:
Total duration: 8 s
Time step: 5 10^{-4} s

Figure 21. Collapse and impact of two water columns in a rectangular tank. Analysis data, geometry and discretization of the columns in two meshes with a total of 3988 3-noded triangles

DOI: 10.1002/fld

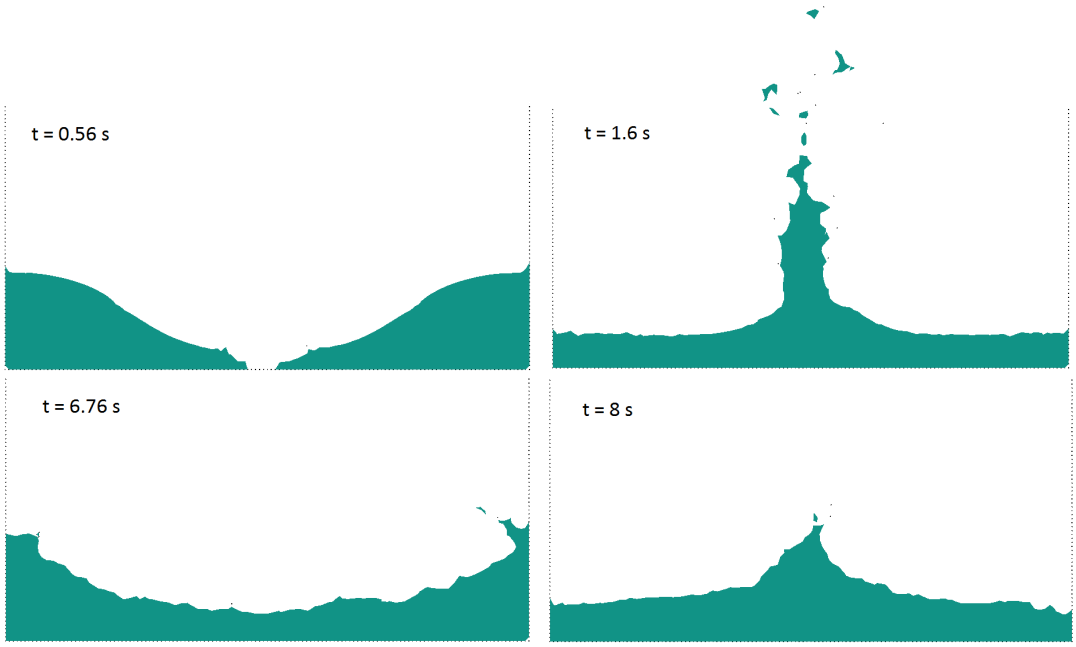

Figure 22. Collapse and impact of two water columns. Snapshots of the evolution of the flow at different times. Results for $\theta = 1$

DOI: 10.1002/fld

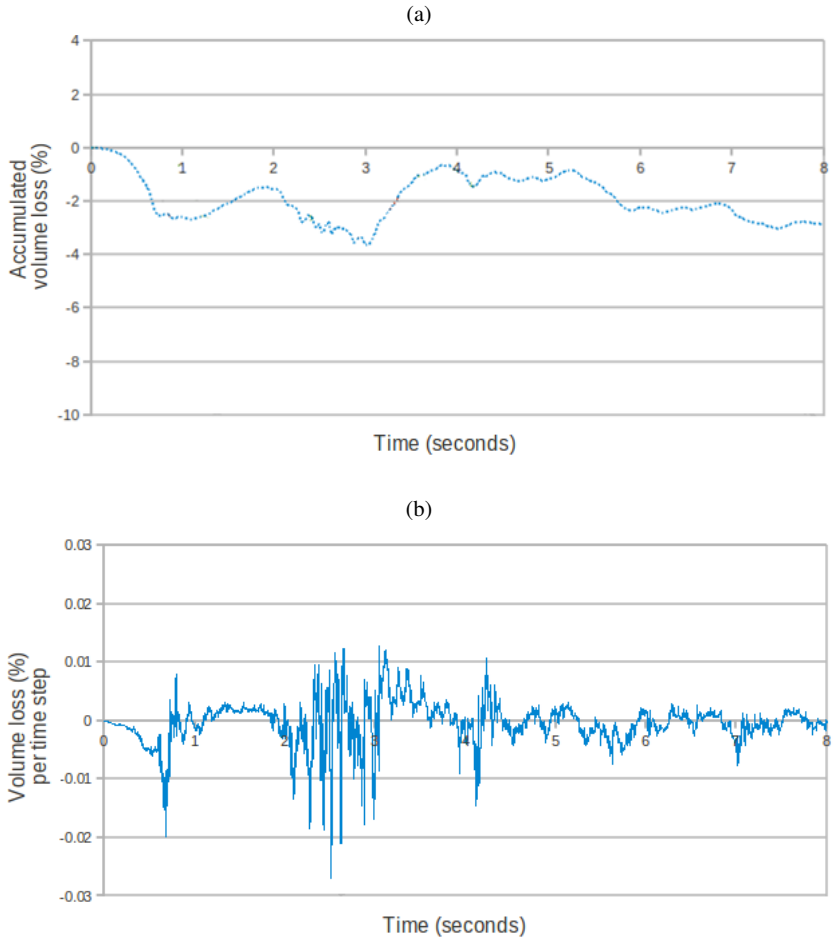

Figure 23. Collapse and impact of two water columns. (a) Accumulated fluid volume (in percentage) over eight seconds of analysis due to the numerical algorithm. (b) Volume loss (in %) per time step. Average volume variation in a time step: $2.24\times10^{-3}\%$. Results for $\theta = 1$

DOI: 10.1002/fld

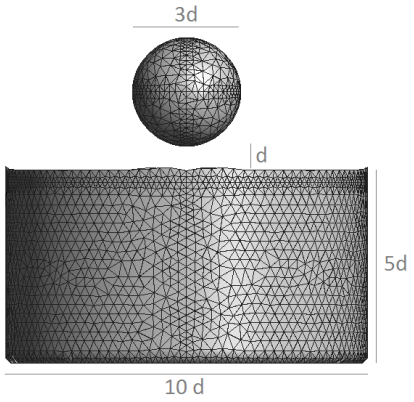

Fluid data:

Viscosity:	10^{-3} Pa s
Bulk Modulus:	2.15 10^{9} Pa
Density:	10^{3} kg/m^{3}

Geometry data:

d:	0.1 m

Mesh data:

Number of nodes:	16935
Number of tetrahedra:	88892
Mean mesh size:	0.03 m

Analysis data:

Total duration:	3s
Time step:	*2* 10^{-4} s

Figure 24. Falling of water sphere in a tank filled with water. Analysis data, geometry and discretization of the sphere and the water in the tank with a total of 88892 4-noded tetrahedra

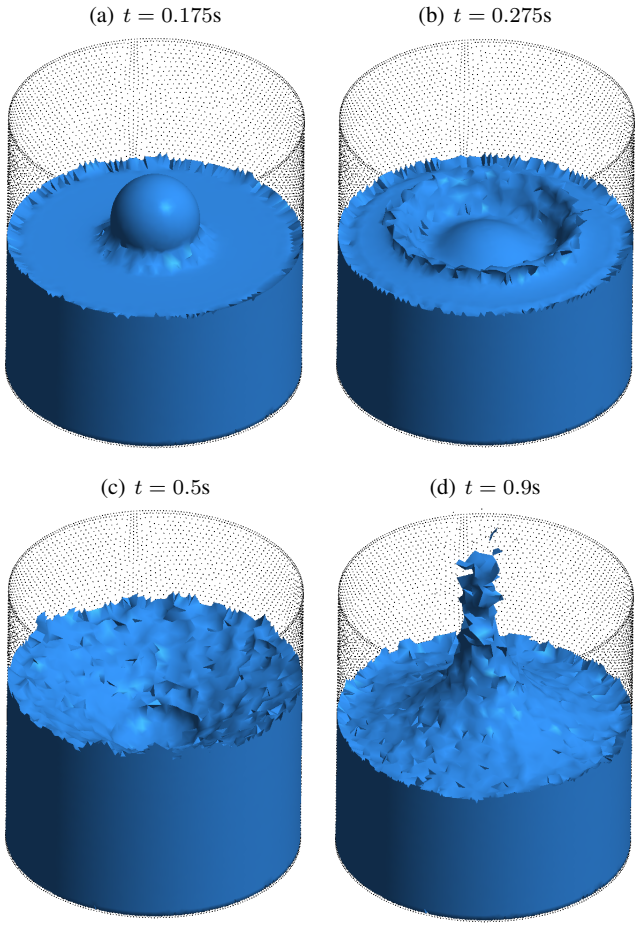

Figure 25. Falling of water sphere in tank containing water. Evolution of the impact and mixing of the two liquids at different times. Results for $\theta = 1$

DOI: 10.1002/fld

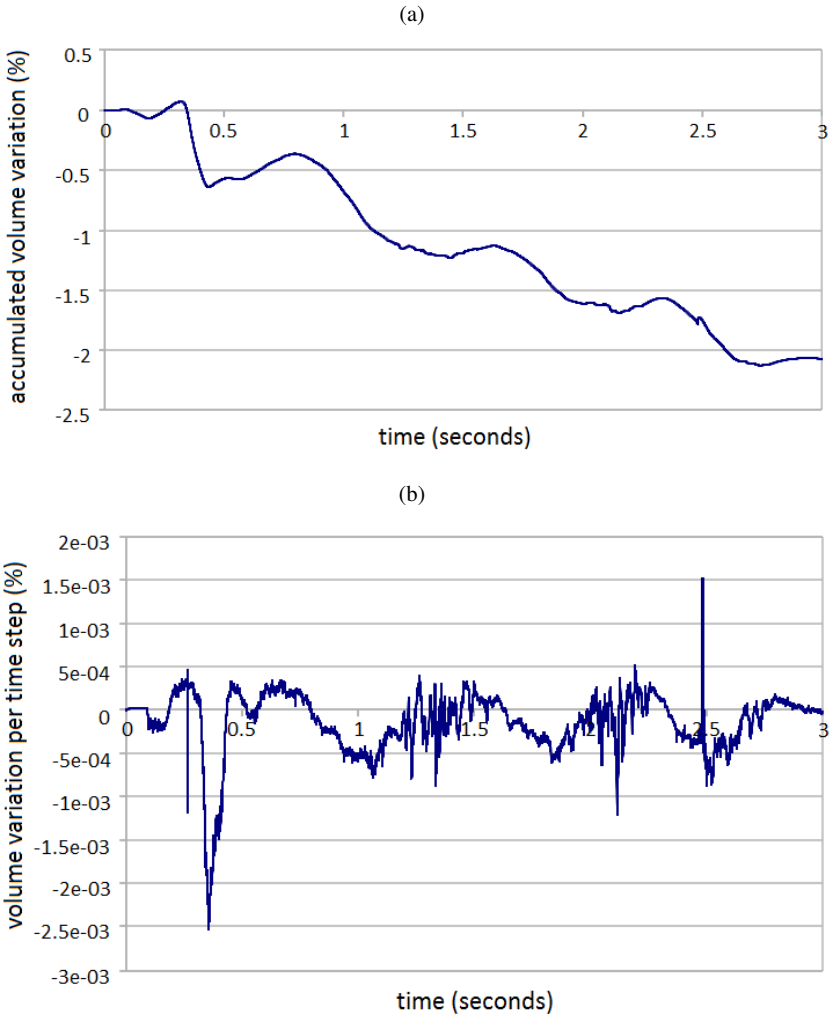

Figure 26. Falling of water sphere in a tank containing water. (a) Accumulated volume over three seconds of analysis due to the numerical algorithm. (b) Volume loss (in %) per time step. Average volume variation in a time step: 2.54×10^{-4}%. Results for $\theta = 1$

11. CONCLUDING REMARKS

We have presented a new FIC-based stabilized finite element method for Lagrangian analysis of incompressible flows that has excellent mass preservation properties. The method has been successfully applied to the analysis of free-surface incompressible flows using the PFEM and an updated Lagrangian formulation. These problems are more demanding in terms of the mass preservation features of the numerical algorithm. The method proposed has yielded excellent results for a variety of 2D and 3D free surface flow problems solved with the PFEM involving surface waves, water splashing, violent impact of flows with containment walls and mixing of fluids.

The method proposed can be easily extended to Stokes flow problems, as well as to Navier-Stokes problems using standard Eulerian formulations.

DOI: 10.1002/fld

ACKNOWLEDGEMENTS

This research was supported by project SEDUREC of the Consolider Programme of the Ministerio de Educación y Ciencia of Spain, Advanced Grant projects SAFECON and REALTIME of the European Research Council and the HFLUIDS project of the National Research Programme of Spain.

REFERENCES

[1] T. Belytschko, W.K. Liu, B. Moran, Non linear finite element for continua and structures, 2d Edition, Wiley, 2013.

[2] Carbonell JM, Oñate E, Suárez B (2010) Modeling of ground excavation with the Particle Finite Element Method. Journal of Engineering Mechanics (ASCE) 136(4):455–463

[3] Carbonell JM, Oñate E, Suárez B (2013) Modelling of tunnelling processes and cutting tool wear with the Particle Finite Element Method (PFEM). Accepted in Comput. Mech. (2013) DOI:10.1007/s00466-013-0835-x

[4] Cremonesi M, Frangi A, Perego U (2011) A Lagrangian finite element approach for the simulation of water-waves induced by landslides. Computers & Structures 89:1086–1093

[5] Donea J, Huerta A (2003) Finite element method for flow problems. J. Wiley

[6] Edelsbrunner H, Mucke EP (1999) Three dimensional alpha shapes. ACM Trans. Graphics 13:43–72

[7] Felippa F, Oñate E (2007) Nodally exact Ritz discretizations of 1D diffusion-absorption and Helmholtz equations by variational FIC and modified equation methods. Comput. Mech. 39:91–111

[8] Franci A, Oñate E, Carbonell JM (2013) On the effect of the tangent bulk stiffness matrix in the analysis of free surface Lagrangian flows using PFEM. Research Report CIMNE PI402

[9] Idelsohn SR, Calvo N, Oñate E (2003c) Polyhedrization of an arbitrary point set. Comput. Method Appl. Mech. Engng. 192(22-24):2649–2668

[10] Idelsohn SR, Oñate E, Del Pin F (2004) The particle finite element method: a powerful tool to solve incompressible flows with free-surfaces and breaking waves. Int. Journal for Numerical Methods in Engineering, 61(7):964–989

[11] Idelsohn SR, Marti J, Limache A, Oñate E (2008) Unified Lagrangian formulation for elastic solids and incompressible fluids: Application to fluid-structure interaction problems via the PFEM. Comput Methods Appl Mech Engrg. 197:1762–1776

[12] Idelsohn SR, Mier-Torrecilla M, Oñate E (2009) Multi-fluid flows with the Particle Finite Element Method. Comput Methods Appl Mech Engrg. 198:2750–2767

[13] Idelsohn SR, Oñate E (2010) The challenge of mass conservation in the solution of free-surface flows with the fractional-step method: Problems and solutions. Int. J. Numer. Meth. Biomed. Engng. 26:1313-1330

[14] Idelsohn SR, Nigro N, Limache A, Oñate E (2012) Large time-step explicit integration method for solving problem with dominant convection. Comput. Methods Appl. Mech. Engrg. 217-220:168-185

[15] Koshizuka S, Tamako H, Oka Y (1995) A particle method for incompressible viscous flow with fluid fragmentation. Comput. Fluid Dyn. J. 4 (1):29–46

[16] Larese A, Rossi R, Oñate E, Idelsohn SR (2008) Validation of the Particle Finite Element Method (PFEM) for simulation of free surface flows. Engineering Computations 25(4):385–425

[17] Limache A, Idelsohn, SR, Rossi R, Oñate E (2007) The violation of objectivity in Laplace formulation of the Navier-Stokes equations. Int. J. Numerical Methods in Fluids, 54:639–664.

[18] Oliver X, Cante JC, Weyler R, González C, Hernández J (2007) Particle finite element methods in solid mechanics problems. In: Oñate E, Owen R (Eds) Computational Plasticity. Springer, Berlin, pp 87–103

[19] Oliver X, Hartmann S, Cante JC, Wyler R, Hernández J (2009) A contact domain method for large deformation frictional contact problems. Part 1: theoretical basis. Comput Methods Appl Mech Eng 198:2591–2606

[20] Oñate E (1998) Derivation of stabilized equations for advective-diffusive transport and fluid flow problems. Comput. Meth. Appl. Mech. Engng. 151:233–267

[21] Oñate E (2000) A stabilized finite element method for incompressible viscous flows using a finite increment calculus formulation. Comput Methods Appl Mech Engrg. 182(1–2):355–370

[22] Oñate E, García J (2001) A finite element method for fluid-structure interaction with surface waves using a finite calculus formulation. Comput. Meth. Appl. Mech. Engrg. 191:635–660

[23] Oñate E (2003) Multiscale computational analysis in mechanics using finite calculus: an introduction. Comput. Meth. Appl. Mech. Engrg. 192(28-30):3043–3059

[24] Oñate E, Taylor RL, Zienkiewicz OC, Rojek J (2003) A residual correction method based on finite calculus. Engineering Computations 20:629–658

[25] Oñate E (2004) Possibilities of finite calculus in computational mechanics. Int. J. Num. Meth. Engng. 60(1):255–281

[26] Oñate E, Rojek J, Taylor R, Zienkiewicz O (2004a) Finite calculus formulation for incompressible solids using linear triangles and tetrahedra. Int. J. Numer. Meth. Engng. 59(11):1473–1500

[27] Oñate E, Idelsohn SR, Del Pin F, Aubry R (2004b) The particle finite element method. An overview. Int. J. Comput. Methods 1(2):267–307

[28] Oñate E, M.A. Celigueta, Idelsohn SR (2006a) Modeling bed erosion in free surface flows by the Particle Finite Element Method, Acta Geotechnia 1(4):237–252

[29] Oñate E, Valls A, García J (2006b) FIC/FEM formulation with matrix stabilizing terms for incompressible flows at low and high Reynold's numbers. Computational Mechanics 38 (4-5):440–455

[30] Oñate E, García J, SR Idelsohn, F. Del Pin (2006c) FIC formulations for finite element analysis of incompressible flows. Eulerian, ALE and Lagrangian approaches. Comput. Meth. Appl. Mech. Engng. 195(23-24):3001–3037

[31] Oñate E, Valls A, García J (2007) Computation of turbulent flows using a finite calculus-finite element formulation. Int. J. Numer. Meth. Engng. 54:609–637

[32] Oñate E, Idelsohn SR, Celigueta MA, Rossi R (2008) Advances in the particle finite element method for the analysis of fluid-multibody interaction and bed erosion in free surface flows. Comput. Meth. Appl. Mech. Engng. 197(19-20):1777–1800

[33] Oñate E (2009), Structural analysis with the finite element method. Linear statics. Volume 1. Basis and Solids. CIMNE-Springer

[34] Oñate E, Rossi R, Idelsohn SR, Butler K (2010) Melting and spread of polymers in fire with the particle finite element method. Int. J. Numerical Methods in Engineering, 81(8):1046–1072

[35] Oñate E, Celigueta MA, Idelsohn SR, Salazar F, Suárez B (2011) Possibilities of the particle finite element method for fluid-soil-structure interaction problems. Computational Mechanics, 48(3):307–318.

[36] Oñate E, Nadukandi P, Idelsohn SR, García J, Felippa C (2011) A family of residual-based stabilized finite element methods for Stokes flows. Int. J. Num. Methods in Fluids, 65 (1-3): 106–134

[37] Oñate E, Idelsohn SR, Felippa C (2011) Consistent pressure Laplacian stabilization for incompressible continua via higher-order finite calculus. Int. J. Numer. Meth. Engng, 87 (1-5): 171–195

[38] Oñate E, Nadukandi P, Idelsohn SR (2013) P1/P0+ elements for incompressible flows with discontinuous material properties. Submitted to Comput. Meth. Appl. Mech. Engng.

[39] Oñate E, Carbonell (2013) JM Updated Lagrangian finite element formulation for quasi and fully incompressible fluids. Research Report PI393, CIMNE. Submitted to Comput. Mechanics

[40] Ryzhakov P, Oñate E, Rossi R, Idelsohn SR (2012) Improving mass conservation in simulation of incompressible flows. Int. J. Numer. Meth. Engng. 90(12):1435–1451

[41] Tang B, Li JF, Wang TS (2009) Some improvements on free surface simulation by the particle finite element method. Int. J. Num. Methods in Fluids, 60 (9):1032-1054

[42] Zienkiewicz OC, Taylor RL, Zhu JZ (2005) The finite element method. The basis, 6th Ed., Elsevier

[43] Zienkiewicz OC, Taylor RL (2005) The finite element method for solid and structural mechanics, 6th Ed., Elsevier

[44] Zienkiewicz OC, Taylor RL, Nithiarasu P (2005) The finite element method for fluid dynamics, 6th Ed., Elsevier

DOI: 10.1002/fld

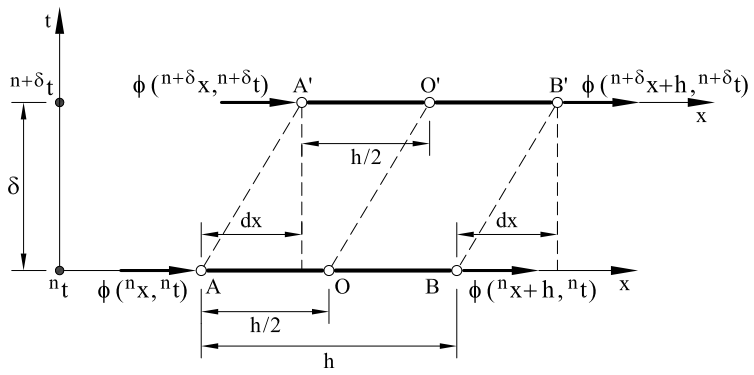

Figure A.1. Evolution of mass flux $\phi = \rho v$ in a tube AB moving in a Lagrangian frame over a time increment δ

APPENDIX A. DERIVATION OF FIC EQUATIONS

Let us consider a 1D tubular domain AB containing a fluid with a density ρ flowing at a velocity v. The domain evolves over a time increment δ to a position A'B'. The horizontal distance $\overline{AA'} = dx = v\delta$. The balance of fluid mass flux through the domain is expressed as

$$\text{Total mass flux}(TMF) = \sum \text{Mass flux-in} \; - \sum \text{Mass flux-out} \; = \text{Accumulated mass} \; (AM) \tag{A.1}$$

From the observation of Figure A.1 and Eq.(A.1) we obtain (using the notation $\phi := \rho v$)

$$TMF = \frac{1}{2}(\phi_A + \phi_{A'}) - \frac{1}{2}(\phi_B + \phi_{B'}) \tag{A.2}$$

Expanding in Taylor series up to third order terms in space around points A and A' we obtain

$$\begin{aligned} \phi_A &= \phi_0 - \frac{1}{2}\phi_0' + \frac{h^2}{8}\phi_0'' - \frac{h^3}{24}\phi_0''' \quad , \quad \phi_B = \phi_0 + \frac{1}{2}\phi_0' + \frac{h^2}{8}\phi_0'' + \frac{h^3}{24}\phi_0''' \\ \phi_{A'} &= \phi_{0'} - \frac{1}{2}\phi_{0'}' + \frac{h^2}{8}\phi_{0'}'' - \frac{h^3}{24}\phi_{0'}''' \quad , \quad \phi_{B'} = \phi_{0'} + \frac{1}{2}\phi_{0'}' + \frac{h^2}{8}\phi_{0'}'' + \frac{h^3}{24}\phi_{0'}''' \end{aligned} \tag{A.3}$$

In the above expressions and in the following dash superscripts denote partial derivatives with respect to the space coordinate x (i.e. $\phi' = \frac{\partial \phi}{\partial x}$), whereas an upper dot denotes time derivatives (i.e. $\dot{\phi} = \frac{\partial \phi}{\partial t}$).

Substituting the expression of ϕ_A, $\phi_{A'}$, ϕ_B and $\phi_{B'}$ into TMF in (A.2) gives

$$TMF \simeq -\frac{1}{2}\left(h\phi_0' + \frac{h^3}{12}\phi_0'''\right) - \frac{1}{2}\left(h\phi_{0'}' + \frac{h^3}{12}\phi_{0'}'''\right) \tag{A.4}$$

On the other hand, we can write

$$\phi_{0'} = \phi_0 + dx\phi_0' + \delta\dot{\phi}_0 \tag{A.5}$$

DOI: 10.1002/fld

Substituting (A.5) into (A.4) gives, neglecting higher order terms (HOT)

$$TMF \simeq -\frac{h}{2}\left(\phi_0 + \frac{h^2}{12}\phi_0^{'''}\right) - \frac{h}{2}\left(\phi_0' dx\phi_0^{''} + \delta\dot{\phi}_0'\right) + \frac{h^2}{12}(\phi_0^{'''} + dx\phi_0^{IV} + \delta\phi_0^{'''}) =$$
$$= -\frac{h}{2}\left[2\phi_0' + dx\phi_0^{''} + \delta\dot{\phi}_0 + \frac{h^2}{6}\phi_0^{'''} + \frac{dxh^2}{12}\phi_0^{IV} + \frac{\delta h^2}{12}\dot{\phi}_0^{'''}\right] \simeq -h\left[\phi_0' + \frac{dx}{2}\phi_0^{''} + \frac{\delta}{2}\dot{\phi}_0 + \frac{h^2}{12}\phi_0^{'''}\right] \tag{A.6}$$

The accumulated mass over time is approximated as

$$AM \simeq \frac{1}{2}\left[\frac{h}{2}(C_A + C_B) + \frac{h}{2}(C_{A'} + C_{B'})\right] = \frac{h}{2}\left[\left(C_0 + \alpha\frac{h^2}{16}C_0^{''}\right) + \left(C_{0'} + \beta\frac{h^2}{16}C_{0'}^{''}\right)\right] \tag{A.7}$$

where $\alpha \geq 1$, $\beta \geq 1$ and C_j denotes the accumulated mass at point j (i.e. $C_0 = \frac{\partial\rho}{\partial t}\Big|_0$).

On the other hand, we can write, following (A.5)

$$C_{0'} = C_0 + dxC_0' + \delta\dot{C}_0 \tag{A.8}$$

Substituting (A.8) into (A.7) gives

$$\begin{aligned} AM \simeq \quad & \frac{h}{2}\left[\left(C_0 + \alpha\frac{h^2}{16}C_0^{''}\right) + \left(C_0 + dxC_0' + \delta\dot{C}_0 + \beta\frac{h^2}{16}C_0^{''}\right) + \text{HOT}\right] \simeq \\ & \simeq h\left[C_0 + \frac{dx}{2}C_0' + \frac{\delta}{2}\dot{C}_0 + (\alpha+\beta)\frac{h^2}{16}C_0^{''}\right] \end{aligned} \tag{A.9}$$

For convenience we choose

$$\alpha + \beta = \frac{4}{3}$$

This gives

$$AM \simeq C_0 + \frac{dx}{2}C_0' + \frac{\delta}{2}\dot{C}_0 + \frac{h^2}{12}C_0^{''} \tag{A.10}$$

Equalling Eqs.(A.6) and (A.10) we obtain the flux balance equation as (after substituting $dx = v\delta$ and $C_0 = \frac{\partial\rho}{\partial t}$)

$$\begin{aligned} -\left(\phi_0' + \frac{v\delta}{2}\phi_0^{''} + \frac{\delta}{2}\dot{\phi}_0' + \frac{h^2}{12}\phi_0^{'''}\right) = \frac{\partial\rho}{\partial t} + \frac{h^2}{12}\frac{\partial^2}{\partial x^2}\left(\frac{\partial\rho}{\partial t}\right) + \\ + \frac{v\delta}{2}\frac{\partial}{\partial x}\left(\frac{\partial\rho}{\partial t}\right) + \frac{\delta}{2}\frac{\partial}{\partial t}\left(\frac{\partial\rho}{\partial t}\right) + \frac{h^2}{12}\frac{\partial^2}{\partial x^2}\left(\frac{\partial\rho}{\partial t}\right) \end{aligned} \tag{A.11}$$

Substituting $\phi_0 = \rho v$ and rearranging terms in (A.11) gives

$$\begin{aligned} \frac{\partial\rho}{\partial t} + \frac{\partial(\rho v)}{\partial x} + \frac{h^2}{12}\frac{\partial^2}{\partial x^2}\left[\frac{\partial\rho}{\partial t} + \frac{\partial(\rho v)}{\partial x}\right] + \\ \frac{\delta}{2}\left[\frac{\partial}{\partial t}\left(\frac{\partial\rho}{\partial t} + \frac{\partial(\rho v)}{\partial x}\right) + v\frac{\partial}{\partial x}\left(\frac{\partial\rho}{\partial t} + \frac{\partial(\rho v)}{\partial x}\right)\right] = 0 \end{aligned} \tag{A.12}$$

DOI: 10.1002/fld

Eq.(A.12) can be rewritten in compact form as

$$\boxed{r_v + \frac{h^2}{12}\frac{\partial^2 r_v}{\partial x^2} + \frac{\delta}{2}\frac{Dr_v}{Dt} = 0} \tag{A.13}$$

with

$$r_v := \frac{\partial \rho}{\partial t} + \frac{\partial(\rho v)}{\partial x} = \frac{D\rho}{Dt} + \rho\frac{\partial v}{\partial x} \tag{A.14}$$

Eqs.(13) and (14) in this paper are obtained by neglecting the time and space derivatives of r_v in Eq.(A.13), respectively.

APPENDIX B. DERIVATION OF THE TANGENT BULK STIFFNESS MATRIX

From Eqs.(12) and (32) we deduce

$$^{n+1}p = ^{n}p + \Delta t\kappa(\theta\, ^{n+1}\varepsilon_v + (1-\theta)^{n}\varepsilon_v) \tag{B.1}$$

where $\kappa = \rho c^2$ is the bulk modulus of the fluid and θ is a positive parameter such that $0 < \theta \leq 1$.

Eq.(B.1) can be rewritten using Eq.(31) as

$$^{n+1}p = ^{n}p + \mathbf{m}^T(\theta\, ^{n+1}\boldsymbol{\varepsilon} + (1-\theta)\, ^{n}\boldsymbol{\varepsilon})\Delta t\kappa \tag{B.2}$$

Substituting the expression of $\boldsymbol{\varepsilon}$ of Eq.(47) into (B.2) gives

$$^{n+1}p = ^{n}p + \mathbf{m}^T\mathbf{B}^T(\theta\, ^{n+1}\bar{\mathbf{v}} + (1-\theta)\, ^{n}\bar{\mathbf{v}})\Delta t\kappa \tag{B.3}$$

Linearization of Eq.(B.3) with respect to the nodal velocity unknowns $^{n+1}\bar{\mathbf{v}}$ gives

$$D_{\bar{v}}\, ^{n+1}p = \theta\Delta t\kappa\mathbf{m}^T\mathbf{B}^T\Delta\bar{\mathbf{v}} \tag{B.4}$$

where $D_{\bar{v}}\, ^{n+1}p$ denotes the directional derivative of the pressure at the updated configuration in the direction of the velocity increments [1, 39], i.e.

$$D_{\bar{v}}\, ^{n+1}p(\mathbf{x}, \bar{\mathbf{v}}) = \left.\frac{d}{d\varepsilon}\right|_{\varepsilon=0} ^{n+1}p(\mathbf{x}, \bar{\mathbf{v}} + \varepsilon\Delta\bar{\mathbf{v}}) \tag{B.5}$$

The linearization of the pressure term in the expression of the virtual power (Eq.(29)) is expressed as

$$D_{\bar{v}}\int_{\Omega^e} \delta\boldsymbol{\varepsilon}^T\mathbf{m}\, ^{n+1}p d\Omega = \int_{\Omega} \delta\boldsymbol{\varepsilon}^T\mathbf{m}(D_{\bar{v}}\, ^{n+1}p)d\Omega \tag{B.6}$$

Making use of Eqs.(B.4) and (47) we finally obtain

$$D_{\bar{v}}\int \delta\boldsymbol{\varepsilon}^T\mathbf{m}\, ^{n+1}p d\Omega = \bar{\mathbf{w}}^T\left(\int_{\Omega}\mathbf{B}^T\mathbf{m}\theta\Delta t\kappa\mathbf{m}^T\mathbf{B}d\Omega\right)\Delta\bar{\mathbf{v}} = \bar{\mathbf{w}}^T\mathbf{K}_v\Delta\bar{\mathbf{v}} \tag{B.7}$$

DOI: 10.1002/fld

where

$$\mathbf{K}_v = \int_\Omega \mathbf{B}^T \mathbf{m} \theta \Delta t \kappa \mathbf{m}^T \mathbf{B} d\Omega \tag{B.8}$$

with $\mathbf{B}$ is defined in Eq.(47).

The elemental expression of the tangent "bulk" matrix $\mathbf{K}_v$ is

$$\mathbf{K}^e_{v_{ij}} = \int_{\Omega^e} \mathbf{B}^{eT}_i \mathbf{m} \theta \Delta t \kappa \mathbf{m}^T \mathbf{B}^e_j d\Omega \quad , \quad i = 1, n \tag{B.9}$$

with $\mathbf{B}^e_i$ defined in Box 1.

APPENDIX C. FRACTIONAL STEP SCHEME

The velocities can be computed from the momentum equation (1) after time integration (using Eq.(2)) as

$$^{n+1}v_i = {}^n v_i + \frac{\Delta t}{\rho}\left(\frac{\partial\, {}^n s_{ij}}{\partial x_j} + \frac{\partial\, {}^{n+1}p}{\partial x_i} + b_i\right) \tag{C.1}$$

In the so-called *first order fractional step* method [5, 44] Eq.(C.1) is split in the following two equations

$$^{n+1}\tilde{v}_i = {}^n v_i + \frac{\Delta t}{\rho}\left(\frac{\partial\, {}^n s_{ij}}{\partial x_j} + b_i\right) \tag{C.2}$$

$$^{n+1}v_i = {}^{n+1}\tilde{v}_i + \frac{\Delta t}{\rho}\frac{\partial\, {}^{n+1}p}{\partial x_i} \tag{C.3}$$

where $^{n+1}\tilde{v}_i$ is the so called fractional velocity [44].

Substituting Eq.(C.3) into the mass balance equation (12a) gives

$$-\frac{1}{\rho c^2}\frac{Dp}{Dt} + \tilde{\varepsilon}_v + \frac{\Delta t}{\rho}\frac{\partial^{2n+1}p}{\partial x_i^2} = 0 \tag{C.4}$$

where $\tilde{\varepsilon}_v = \frac{\partial \tilde{v}_i}{\partial x_i}$.

The weighed residual form of Eq.(C.4) after integrating by parts of the terms involving $\tilde{\varepsilon}_v$ and the pressure, gives using Eq.(C.3)

$$\int_\Omega \frac{q}{\rho c^2}\frac{Dp}{Dt} d\Omega + \int_\Omega \frac{\partial q}{\partial x_i}\tilde{v}_i d\Omega + \int_\Omega \frac{\Delta t}{\rho}\frac{\partial q}{\partial x_i}\frac{\partial\, {}^{n+1}p}{\partial x_i} d\Omega - \int_{\Gamma_t} q\, {}^{n+1}v_n d\Gamma = 0 \tag{C.5}$$

where q are the pressure test functions and $^{n+1}v_n$ is the normal velocity to the Neumann boundary Γ_t (typically the free boundary in the fluid).

Eqs.(C.2), (C.3) and (C.5) are discretized using the Galerkin FEM in the standard manner [5, 42, 44].

The three-steps of the first order fractional step method are:

Step 1. Compute the nodal fractional velocities from Eq.(C.2).

Step 2. Compute the nodal pressures from Eq.(C.5).

Step 3. Compute the nodal velocities from Eq.(C.3).

DOI: 10.1002/fld

Typically the nodal velocities are prescribed in the Step 3 while the fractional velocities are left unprescribed in the solution of Step 1.

The computation of the pressure in Step 2 via Eq.(C.5) requires prescribing the pressure at the free boundary to avoid the singularity of the equation system involving the inverse of a Laplacian matrix.

The normal velocities ${}^{n+1}v_n$ can be substituted by ${}^{n}v_n$ in order to make the scheme fully explicit. A more accurate implicit scheme can be obtained by iterating between Steps 2 and 3 until convergence of the nodal velocities and pressures is achieved.

An alternative *second order fractional step* method can be obtained by writing Eqs.(C.3) and (C.4) as

$$ {}^{n+1}\tilde{v}_i = {}^{n}v_i + \frac{\Delta t}{\rho}\left(\frac{\partial\, {}^{n}s_{ij}}{\partial x_j} + \frac{\partial\, {}^{n}p}{\partial x_i} + b_i\right) \tag{C.6} $$

$$ {}^{n+1}v_i = {}^{n+1}\tilde{v}_i + \frac{\Delta t}{\rho}\frac{\partial \Delta p}{\partial x_i} \quad \text{with } \Delta p = {}^{n+1}p - p \tag{C.7} $$

Eq.(C.5) has the same form with the pressure increment Δp substituting the pressure ${}^{n+1}p$. The solution scheme follows the three steps described above for computation of the nodal velocities and the nodal pressure increments.

The second order fractional step is typically more accurate from the first order one. However, it requires additional stabilization as the Laplacian of pressure term in Eq.(C.5) vanishes as $\Delta p \to 0$ [44].

Further details of the fractional step method can be found in [5, 44] and the references therein.

DOI: 10.1002/fld